



HAL
open science

Coupled heat and mass transfer in shallow caves: interactions between turbulent convection, gas radiative transfer and moisture transport

B. Qaddah, Laurent Soucasse, Frédéric Doumenc, Sophie Mergui, Philippe
Riviere, Anouar Soufiani

► To cite this version:

B. Qaddah, Laurent Soucasse, Frédéric Doumenc, Sophie Mergui, Philippe Riviere, et al.. Coupled heat and mass transfer in shallow caves: interactions between turbulent convection, gas radiative transfer and moisture transport. *International Journal of Thermal Sciences*, 2023, 194, pp.108556. 10.1016/j.ijthermalsci.2023.108556 . hal-04172286

HAL Id: hal-04172286

<https://hal.science/hal-04172286>

Submitted on 27 Jul 2023

HAL is a multi-disciplinary open access archive for the deposit and dissemination of scientific research documents, whether they are published or not. The documents may come from teaching and research institutions in France or abroad, or from public or private research centers.

L'archive ouverte pluridisciplinaire **HAL**, est destinée au dépôt et à la diffusion de documents scientifiques de niveau recherche, publiés ou non, émanant des établissements d'enseignement et de recherche français ou étrangers, des laboratoires publics ou privés.

Highlights

Coupled heat and mass transfer in shallow caves: interactions between turbulent convection, gas radiative transfer and moisture transport

B. Qaddah, L. Soucasse, F. Doumenc, S. Mergui, Ph. Rivière, A. Soufiani

- The thermal behavior of a shallow cave presents strong similarities with the simpler academic configuration of the differentially heated cavity.
- Gas radiation increases the flow circulation in the cavity through wall–gas radiative exchanges and significantly modifies the wall radiative flux.
- In the energy balance at the walls, the radiative flux overcomes the conductive flux. However, the addition of conduction and latent heat fluxes, both driven by convection, prevails over radiation in some regions of the cavity.
- The region of the cavity roof at the shortest distance from the ground undergoes the maximum heat and mass fluxes, with condensation resulting in limestone dissolution.

Coupled heat and mass transfer in shallow caves: interactions between turbulent convection, gas radiative transfer and moisture transport

B. Qaddah^a, L. Soucasse^a, F. Doumenc^{b,c}, S. Mergui^{b,c}, Ph. Rivière^a, A.
Soufiani^a

^a*Laboratoire EM2C, CNRS, CentraleSupélec, Université Paris-Saclay, 8-10 rue Joliot
Curie, 91192 Gif-sur-Yvette, France*

^b*Université Paris-Saclay, CNRS, FAST, 91405, Orsay, France*

^c*Sorbonne Université, UFR 919, 4 place Jussieu, F-75252, Paris Cedex 05, France*

Abstract

Understanding and predicting the microclimate of shallow caves is a key issue for the conservation of parietal art. In order to determine the dominant mechanisms of heat transfer in a configuration close to that of painted caves, we performed numerical simulations of a parallelepiped cavity whose dimensions and depth are of the order of 10 m. This simple geometry allowed us to use a detailed model including turbulent natural convection, gas radiation, along with vapor transport and latent heat fluxes resulting from condensation and evaporation on the walls.

Gas radiation increases the flow circulation in the cavity through wall–gas radiative exchanges and significantly modifies the wall radiative flux. Conversely, the wall conductive flux remains unchanged (a non trivial behavior reported in the literature about the differentially heated cavity). In the energy balance at the walls, the radiative flux overcomes the conductive flux. However, the addition of conduction and latent heat fluxes, both driven by convection, prevails over radiation in some regions of the cavity.

Heat and mass fluxes are maximum in areas of the cavity roof where the distance from the ground is the shortest. Due to the asymmetry induced by the inversion of the vertical temperature gradient twice a year, net condensation resulting in limestone dissolution is expected in these areas, whereas

Email address: doumenc@fast.u-psud.fr (F. Doumenc)

the other regions of the cave undergo net evaporation resulting in limestone deposition. The orders of magnitude of the condensation flux (a few microns per day) and of the retreat velocity of the wall (a few tenth of a micron per year) are in line with the field data available in the literature.

Keywords: Shallow caves, Heat and mass transfer, Turbulent natural convection, Gas radiation, Condensation, Corrosion

1. Introduction

Predicting cave microclimate is essential in many fields as diverse as paleoclimate reconstruction [1], tunneling [2], or the study of subterranean fauna and flora [3]. This is also a critical issue for the conservation of cave paintings. Indeed, the exceptional state of conservation of parietal prehistoric paintings is mainly due to the high stability of cave microclimate. However, cave microclimate can be disturbed in various ways. A visitor influx results in a sudden increase of temperature, carbon dioxide (CO_2) concentration and humidity [4, 5, 6]. Cave modifications required to accommodate visitors (artificial ventilation [5], creation of a large entrance [7], removal of a detritic scree acting as a thermal buffer [8]) may increase heat and mass exchanges with the external environment. The potential consequences of these disturbances are manifold. The microbiological balance can be disturbed, resulting in the formation of stains on the walls [9]. CO_2 fluctuations may result in the corrosion of limestone walls by dissolution of calcium carbonate (CaCO_3) or, conversely, deposition of CaCO_3 films. CaCO_3 dissolution or deposition can also be triggered by condensation and evaporation [10, 11, 12]. Moreover, condensation is at the core of other issues. First, it can increase the risk of growth of unwanted microbiological species as fungi [13, 14]. Second, the possibility to form vermiculations by water condensation was recently demonstrated through laboratory experiments [15]. Vermiculations are natural patterns commonly observed on cave walls [16]. The formation of vermiculations in painted caves triggers the migration of painting pigments along the wall [17], resulting in serious damages to the paintings [18].

A deep understanding of heat transfer within the cave and between the cave and the external environment is thus required for a rational management of painted caves and to achieve proper remediation when it becomes necessary (e.g., by designing and building artificial thermal buffers [8]). In this article we focus on closed shallow caves, i.e., caves with negligible air ex-

30 changes with the external environment and located at depths ranging from
31 a few meters to 20 m. Many painted caves fall in this category, including the
32 famous Lascaux Cave in France [7] and Altamira Cave in Spain [19]. For
33 such caves, heat transfer between the ground level and the cave is mainly
34 due to heat conduction [20, 19], while natural convection and infrared ra-
35 diation occur inside the cave. In the range of depth considered here, daily
36 temperature fluctuations are completely damped by heat diffusion in the rock
37 layer between the ground level and the cave, but yearly fluctuations are still
38 measurable. Due to the complex geometry of the cave and depth variations
39 all along the cave, spatial temperature differences at a given time are also
40 expected. For instance, the amplitude of the yearly temperature variations
41 in the Hall of Bull in Lascaux Cave is of the order of a few tenth of de-
42 grees [21, 22]. The spatial temperature variations at a given time inside the
43 cave are of the same order [23].

44 Such temperature variations might seem very small. However, in a cave
45 of 5 m height with a temperature difference of 0.1 K between the floor and
46 the roof, the Rayleigh number is of the order of 10^9 , value at which turbulent
47 natural convection is expected. This was confirmed through the resolution
48 of Navier–Stokes equations based on large eddy simulations (LES) [24], a
49 method which allows the accurate prediction of the turbulent flow structure.
50 In this recent work, we considered the case of a parallelepiped cavity whose
51 size and depth roughly mimic the dimensions of the Hall of Bull in Lascaux
52 Cave. Assuming that the cave atmosphere was dry (no release of latent heat)
53 and transparent to the infrared radiation, we compared the wall convective
54 and radiative heat fluxes. We showed that, with the assumptions mentioned
55 above, wall-to-wall radiation was the dominant mechanism. But the real
56 situation is further complicated by two factors typical of cave atmospheres.

- 57 1. In weakly ventilated caves, the natural infiltration of water through the
58 pores and the fissures of the rock results in relative humidity close to
59 100% [19, 8]. Under these conditions, small temperature differences are
60 sufficient to produce significant evaporation and condensation fluxes,
61 resulting in latent heat release on the walls and vapor transfer from the
62 hot to the cold spots of the cave.
- 63 2. The amount of CO_2 in soils is controlled by plant roots, microorgan-
64 isms respiration and organic matter decomposition [25]. The CO_2 is
65 transferred from soils to caves in gaseous form or after dissolution in
66 water. Whereas the molar fraction of CO_2 in the atmosphere is ap-

67 proximately 0.04%, it can reach several percent in caves [21]. Due to
68 the presence of saturated water vapor and CO₂, the cave atmosphere
69 should probably not be considered as transparent for the infrared ra-
70 diation. Indeed, the emission and absorption of radiation affect the
71 temperature of a radiating fluid, which in turn controls the buoyant
72 motion. Gas radiation has been shown to significantly interact with
73 convection in various configurations including plumes generated by a
74 localized heat source [26], the Rayleigh–Bénard cell [27] or the dif-
75 ferentially heated cavity [28, 29]. Among the academic configurations
76 studied in the literature, the latter is the closest to ours. It consists
77 of two vertical, parallel, isothermal walls surrounded by four adiabatic
78 walls. Soucasse *et al* [30, 31] and Kogawa *et al* [32, 33] simulated the
79 turbulent natural convection coupled to wall and gas radiation in a dif-
80 ferentially heated cubical cavity. The cavity was filled with a mixture
81 of air, water vapor and CO₂. These authors observed that wall-gas
82 radiative exchanges induced a thickening of vertical boundary layers
83 resulting in a strong intensification of the global circulation in the cav-
84 ity and an increase of the turbulence level. However, conductive fluxes
85 through the walls were little modified by gas radiation. Soucasse *et al*
86 worked at Rayleigh numbers ranging from $Ra = 3 \times 10^7$ to 3×10^9 .
87 The averaged transmissivity based on the cavity size and weighted by
88 the Planck function at room temperature was equal to 0.83. The study
89 of Kogawa *et al* [32, 33] was performed at Rayleigh number 1.5×10^9
90 with different concentrations of water vapor and CO₂ corresponding to
91 transmissivities of 0.89 and 0.64. They found results similar to those of
92 Soucasse *et al* (enhancement of the global circulation with little effect
93 on the wall conductive fluxes).

94 The temperature field inside a cave thus results from a complex interplay
95 between heat conduction in the surrounding rock and, inside the cave, turbu-
96 lent natural convection resulting in heat and mass convective transfer, heat
97 conduction and latent heat release on the walls, and radiative transfer be-
98 tween the cave walls and between the cave walls and the cave atmosphere. All
99 of these mechanisms are strongly coupled. The main objective of the present
100 article is to assess their relative significance, determine those that are dom-
101 inant, and those that can be neglected with no significant loss of accuracy.
102 For this purpose, we rely on the same approach as already implemented in
103 ref. [24], but we now consider that the cave atmosphere is humid and radiant.

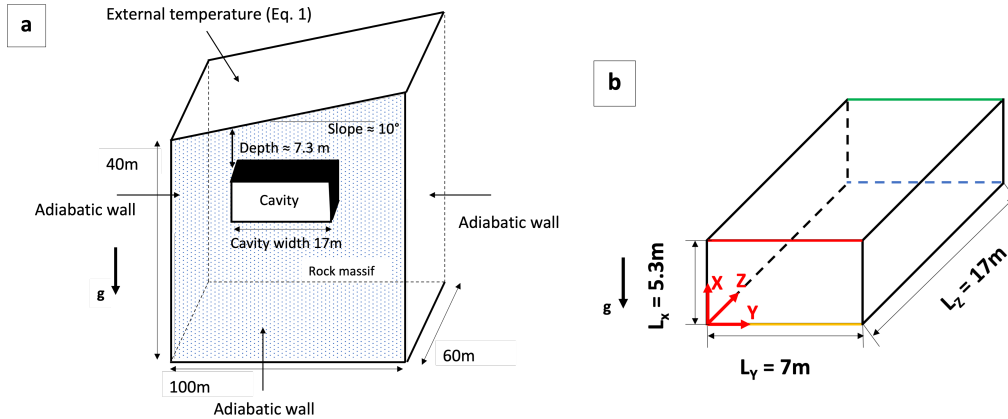


Figure 1: a) General geometry of the rock mass (not at scale). b) Detailed diagram of the cavity, with the definition of the axes. Red, yellow, green and blue lines correspond to the left upper ($Z = 0$ and $X = L_X$), left bottom ($Z = 0$ and $X = 0$), right upper ($Z = L_Z$ and $X = L_X$) and right bottom ($Z = L_Z$ and $X = 0$) edges, respectively

104 Numerical simulations are performed in the simplified case of a parallelepiped
 105 cavity, which allows the use of an accurate mathematical model in which the
 106 coupling between radiative transfer and convective heat and mass transports
 107 inside the cavity are strictly implemented. This approach provides the orders
 108 of magnitude of the various heat and mass fluxes through the cave walls, in-
 109 cluding the time and location of condensation events. Simplifications to be
 110 made in future models of closed shallow caves are deduced from these results.

111 The article is organized as follows. The problem statement and the phys-
 112 ical assumptions used in the model are detailed in Sec. 2. The governing
 113 equations and the numerical methods are presented in sections 3 and 4. Sec-
 114 tion 5 describes the effects of the solutal buoyancy and the gas radiation on
 115 the flow pattern. The consequences on heat and mass fluxes through the
 116 cavity walls are reported in Sec. 6.

117 2. Problem statement

118 2.1. Geometry and boundary conditions

119 We consider the same confined parallelepiped cavity as in our previous
 120 work [24]. The cavity is embedded in the rock mass displayed in Fig. 1a.
 121 The ground surface is inclined at 10° from the horizontal direction. Its tem-

122 perature follows the external temperature

$$T_{ex}(t) = T_m + A \cos\left(2\pi\frac{t}{\tau}\right), \quad (1)$$

123 where $\tau = 1$ year is the period, $T_m = 12^\circ\text{C}$ is the annual average external
124 temperature and $A = 8^\circ\text{C}$ is the amplitude of the temperature variations
125 (these values of T_m and A are typical of the climate conditions in south-west
126 of France). As we only consider the periodic regime, we arbitrarily assume
127 that the initial time corresponds to the hottest temperature of the year that
128 takes place in July. The other external boundaries of the rock mass are all
129 adiabatic. The left upper edge of the cavity is located at a depth of 7.3 m.
130 The cave dimensions are the height $L_X = 5.3$ m, the width $L_Y = 7$ m and the
131 length $L_Z = 17$ m. The axes \mathbf{X} , \mathbf{Y} and \mathbf{Z} are displayed in Fig. 1b. $\mathbf{g} = -g\mathbf{X}$
132 is the gravitational acceleration field.

133 Ideally, we should consider a 1-year periodic problem including heat con-
134 duction in the rock fully coupled with radiation and turbulent natural convec-
135 tion inside the cave. However, a one-year simulation of the Navier–Stokes
136 equations in the turbulent regime is not practicable with current compu-
137 tational resources. In our previous work [24], this difficulty was overcome
138 by defining a large-scale model including heat conduction in the rock and
139 radiative transfer between the cavity walls, but disregarding natural convec-
140 tion inside the cavity. Solving the 1-year periodic regime of this large-scale
141 model yielded temperature fields of the cavity walls throughout the year (see
142 the results for May and November in Fig. 2). In a second step, these wall
143 temperature fields at six selected times of the year were used as boundary
144 conditions to solve the natural convection problem inside the cavity (Cheby-
145 shev pseudo-spectral method associated to large eddy simulations (LES)
146 with a spectral vanishing viscosity (SVV) model). The Rayleigh number
147 $Ra = g\beta_T\Delta TL_X^3/(\alpha\nu)$ was based on the difference ΔT between the maxi-
148 mum and the minimum wall temperatures (with g the gravity acceleration,
149 β_T the thermal expansion coefficient, α the thermal diffusivity and ν the
150 kinematic viscosity). Ra ranged from 2.1×10^9 (in August and February)
151 to 8.4×10^9 (in May and November). Two flow regimes were identified. A
152 one-cell flow regime with a large level of turbulence and an isothermal core
153 (strong thermal mixing) was observed when the vertical gradient was nega-
154 tive (roof colder than the floor). This happened in March, May and August.
155 Conversely, a multiple-cell flow regime with a lower turbulence level and a
156 thermal stratification in the core was observed when the vertical gradient

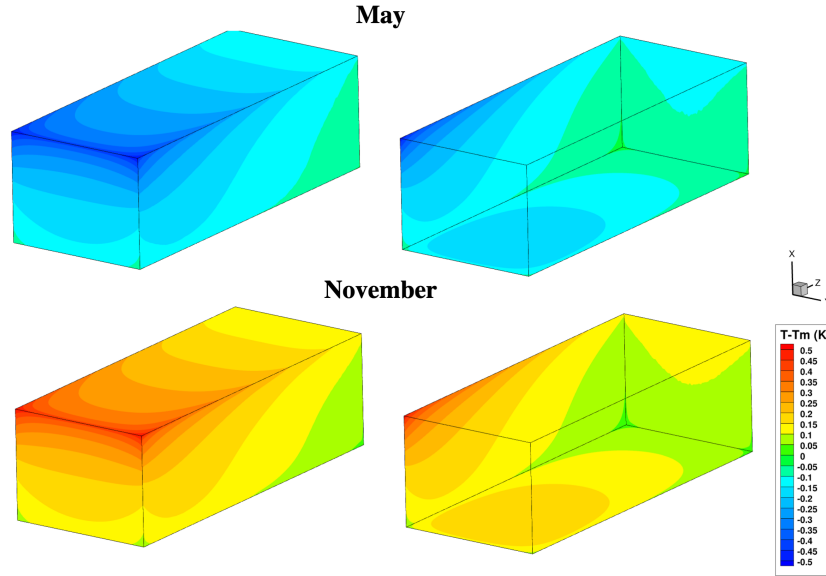


Figure 2: Wall temperature fields $T - T_m$ computed from the large-scale model for May and November (from ref. [24]). The left panel corresponds to the top ($X = L_X$), left ($Z = 0$) and front ($Y = L_Y$) cave walls. The right panel corresponds to the bottom ($X = 0$), right ($Z = L_Z$) and rear ($Y = 0$) cave walls. The difference ΔT between the maximum and the minimum wall temperatures is 0.492 K in both cases.

157 was positive, in September, November and February. In both regimes, heat
 158 transfer at the cavity walls was dominated by the radiative flux. This *a pos-*
 159 *teriori* justified that natural convection was neglected in the determination of
 160 the thermal boundary conditions at the cave walls by the large-scale model.

161 We follow the same approach in the present work to determine the effect
 162 of vapor transfer and gas radiation. We assume that the large-scale model
 163 provides realistic temperature distributions on cave walls, and we use them
 164 as boundary conditions. The natural convection problem, including heat and
 165 mass transfer coupled to radiation, is solved by LES with the SVV model.
 166 We focus on May and November, both months associated with the largest
 167 temperature gradients, as typical of the one-cell flow regime and the multiple-
 168 cell flow regime, respectively. The physical assumptions needed to model the
 169 mass transfer and the gas radiation are detailed in sections 2.2 and 2.3 below.

170 *2.2. Mass transfer, condensation and evaporation*

171 The density of the cave atmosphere mainly depends on three parameters:
172 the temperature, the water vapor concentration and the CO₂ concentration.
173 Therefore, the gradient of each of these three quantities may contribute to the
174 buoyancy that drives natural convection. However, the dynamics of the CO₂
175 is an intricate problem. Several mechanisms with different time scales may be
176 responsible for the transfer of CO₂ from the soil to the cave [34, 23]. As a first
177 step, uniform CO₂ concentration will be considered in the present work. We
178 thus assume that the buoyancy is only due to the gradients of temperature
179 and water vapor concentration. The resulting thermal and solutal buoyant
180 forces add up since the water vapor content increases with temperature and
181 water vapor is lighter than dry air. The relative contributions of these two
182 factors will be assessed.

183 We investigate the case of cave walls entirely covered with a thin wa-
184 ter film whose origin may be percolation and/or condensation. In general,
185 condensation may also occur in the gas phase, resulting in the formation
186 of clouds. Clouds have been observed in caves, in certain configurations
187 (e.g., the mixing of two air streams at different temperatures [35]). However,
188 aerosols acting as nucleation points are necessary to initiate the formation of
189 droplets. The presence of such aerosols in caves is strongly correlated to the
190 ventilation and the visitor disruptions [36]. In weakly ventilated caves with
191 a reduced number of visitors, the presence of significant aerosols lasting on
192 long times is unlikely. We thus disregard condensation in the gas phase, and
193 we assume that evaporation and condensation take place on the walls only.

194 The high dilution of the water vapor in the cave atmosphere allows to
195 simplify the derivation of the condensation/evaporation flux at the cave
196 wall. Indeed, the saturated vapor pressure $P_{sat} \simeq 14.03$ mbar at temperature
197 $T_m = 12^\circ\text{C}$ [22] and the atmospheric pressure $P_{atm} \simeq 1013$ mbar yield the
198 water vapor molar fraction $x_w \simeq P_{sat}(T_m)/P_{atm} \simeq 0.014$, much lower than
199 1. In such a situation, the condensation or evaporation fluxes are driven by
200 the diffusion of the dilute vapor through the non-condensable gases (air and
201 CO₂ in our case). The kinetic resistance at the liquid–gas interface can be
202 neglected compared to the transfer resistance of the solutal boundary layer
203 in the gas phase, and the local thermodynamic equilibrium is assumed at
204 the liquid–gas interface (see for instance Ref. [37] for a detailed discussion on
205 the physical mechanisms driving evaporation or condensation). Therefore,
206 the water vapor is always saturated at the walls, and can be slightly under-
207 saturated or supersaturated in the core of the gas phase. In the simulation

208 results, the volume-averaged absolute value of the deviation from saturation
 209 was always lower than 10^{-3} .

210 2.3. Radiative properties of the cave atmosphere

211 With the assumption of a clean atmosphere, there is no scattering due
 212 to suspended particles. The radiative properties of the cave atmosphere
 213 thus reduce to the absorption coefficient κ_ν , which depends on the radiation
 214 wavenumber ν and the atmosphere composition. Fig. 3 shows the absorption
 215 spectrum of air mixed with CO₂ and water vapor at molar fractions $x_{\text{CO}_2} =$
 216 0.02 and $x_w = 0.014$, respectively. The temperature is the yearly averaged
 217 atmospheric temperature $T_m = 285.15$ K and the total pressure is $P_{\text{atm}} =$
 218 1 atm. The molar fraction of water vapor corresponds to saturated vapor at
 219 temperature T_m . The absorption spectrum was calculated from a line by line
 220 approach using the HITRAN database [38].

221 The significance of gas radiation compared to wall radiation can be esti-
 222 mated from the transmissivity τ_g defined as

$$\tau_g = \frac{\pi}{4\sigma_{SB}T_m^3} \int_{\nu} \exp(-\kappa_\nu \ell) \frac{dI_\nu^0}{dT}(T_m) d\nu, \quad (2)$$

223 where σ_{SB} and $I_\nu^0(T_m)$ are the Stefan-Boltzmann constant and the Planck
 224 function, respectively. The transmissivity τ_g is the net radiative flux ex-
 225 changed by two black walls through an optical path of mean beam length ℓ ,
 226 scaled by the net radiative flux through a transparent medium (the radiative
 227 transfer temperature dependence has been linearized). The relative contri-
 228 bution of gas radiation compared to surface-to-surface radiation is expected
 229 to be negligible for $\tau_g \simeq 1$ and dominant for $\tau_g \ll 1$.

230 τ_g is displayed in Fig. 4 for the three values $x_{\text{CO}_2} = 0, 0.02$ and 0.1 , at
 231 constant water vapor molar fraction $x_w = 0.014$. A rough estimation of the
 232 transmissivity between two opposite walls of the cave can be obtained from
 233 Fig. 4 assuming a characteristic size of 10 m (the order of magnitude of the
 234 cavity size, see Fig. 1). The corresponding transmissivity decreases from 0.81
 235 to 0.66 when the CO₂ molar fraction increases from 0 to 0.1. These values
 236 suggest a non negligible contribution of gas radiation to the radiative transfer.
 237 Furthermore, the results obtained by Soucasse *et al* [30, 31] and Kogawa *et*
 238 *al* [32, 33] for the differentially heated cavity with similar Rayleigh numbers
 239 and transmissivities (see Sec. 1) also suggest a significant modification of the
 240 flow pattern by gas radiation. Figure 4 indicates an increase of these two

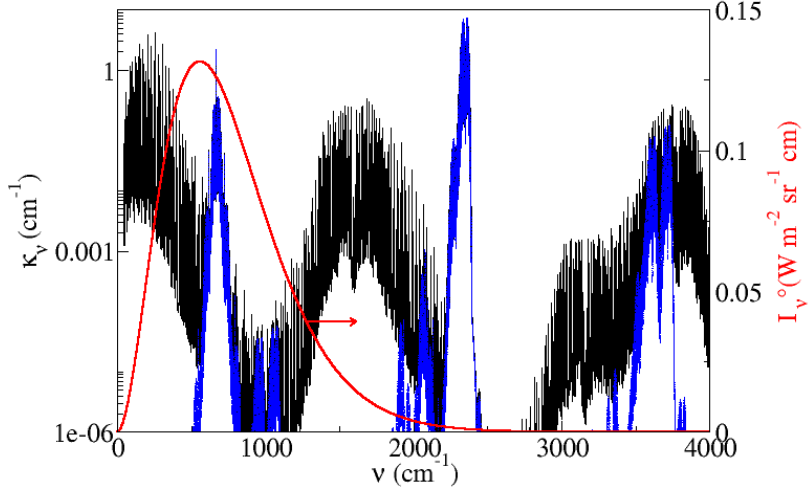


Figure 3: Absorption coefficient spectrum of the cave atmosphere considered as a mixture of air, saturated water vapor (molar fraction $x_w = 0.014$) and CO_2 (molar fraction $x_{\text{CO}_2} = 0.02$) at temperature $T_m = 285.15 \text{ K}$ and atmospheric pressure (black); CO_2 contribution (blue); Planck function $I_v^\circ(T_m)$ (red).

241 effects (contribution of gas radiation to radiative transfer and modification
 242 of the flow pattern) with the CO_2 level. In the following, we set $x_{\text{CO}_2} = 0.02$,
 243 a high level of CO_2 commonly observed in caves. The corresponding value
 244 of τ_g is approximately 0.7.

245 3. Governing equations

246 3.1. Natural convection

247 In the parallelepiped cavity displayed in Fig. 1b, we consider the natural
 248 convection flow of a humid air mixture caused by both temperature and
 249 moisture gradients. Conservation equations for mass, momentum, energy
 250 and water vapor concentration write

$$\nabla \cdot \mathbf{u} = 0, \quad (3)$$

$$\frac{\partial \mathbf{u}}{\partial t} + \mathbf{u} \cdot \nabla \mathbf{u} = -\frac{1}{\rho_0} \nabla p + \beta_T (T_0 - T) \mathbf{g} + \beta_c (c_0 - c) \mathbf{g} + \nu \nabla^2 \mathbf{u}, \quad (4)$$

$$\frac{\partial T}{\partial t} + \mathbf{u} \cdot \nabla T = \alpha \nabla^2 T + \frac{1}{\rho_0 C_P} \mathcal{P}_{\text{rad}}, \quad (5)$$

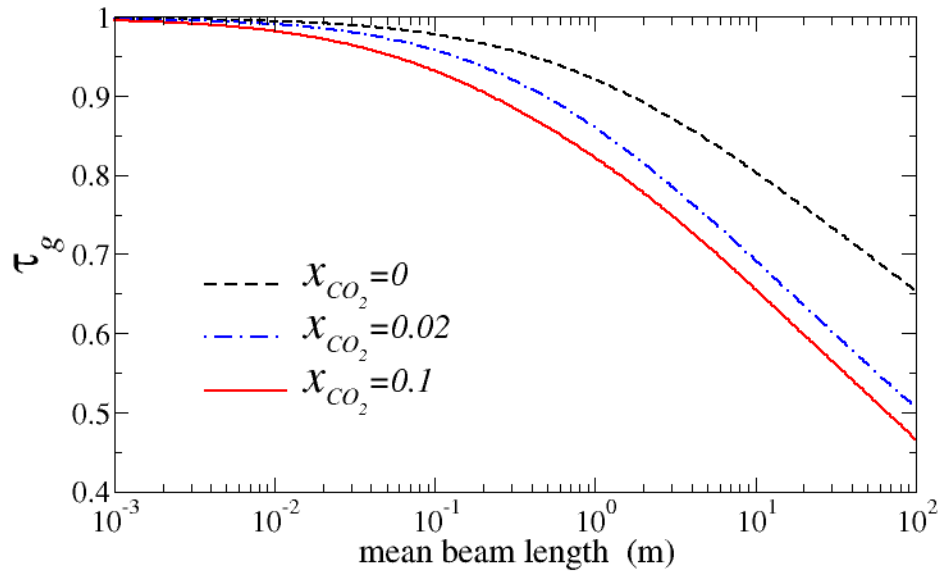


Figure 4: Effect of the CO_2 concentration on the transmissivity τ_g defined in Eq. (2) as a function of the mean beam length ℓ , at temperature $T_m = 285.15\text{ K}$ and atmospheric pressure, for saturated water vapor (molar fraction $x_w = 0.014$).

$$\frac{\partial c}{\partial t} + \mathbf{u} \cdot \nabla c = D \nabla^2 c, \quad (6)$$

254 where \mathbf{u} , p , T and c are respectively the velocity vector, the motion pressure,
 255 the temperature, and the water vapor mass concentration. The radiative
 256 power \mathcal{P}_{rad} in the energy balance (Eq. (5)) corresponds to the emission and
 257 absorption of radiation by the fluid and will be discussed in details in Sec. 3.2.
 258 There is no source term due to phase change in transport equations (5)-
 259 (6) because phase change is supposed to take place on the walls only (see
 260 section 2.2). It should be noted here that subgrid terms complement Eqs. (4)-
 261 (6) when the LES approach is employed (see Sec. 4.1).

262 The boundary conditions at the cave walls are defined as follows. We
 263 assume that the water film lying on the walls is thin enough to neglect: (1)
 264 its velocity compared to the air velocity, (2) its conductive thermal resistance
 265 compared to the boundary layer resistance in the gas phase. With the ad-
 266 ditional assumptions of no slip and local thermodynamic equilibrium on the
 267 walls, we get:

$$\mathbf{u} = \mathbf{0}, \quad T = T_w \quad \text{and} \quad c = c_{\text{sat}}(T_w), \quad (7)$$

268 where T_w is the wall temperature given by the large scale model (see Sec. 2.1
 269 and Fig. 2), and $c_{\text{sat}}(T_w)$ is the concentration of the saturated water vapor at
 270 temperature T_w . Because of the small temperature range considered in the
 271 simulations (approximately 1 K), we assume that $c_{\text{sat}}(T)$ varies linearly with
 272 the temperature T [22]:

$$c_{\text{sat}}(T) = c_{\text{sat}}(T_m) + \beta(T - T_m), \quad (8)$$

273 where β is the derivative of $c_{\text{sat}}(T)$ at $T = T_m$ (see table 1).

274 The physical properties of the fluid are listed in table 1. Following the
 275 Boussinesq approximation, the fluid density is assumed constant except in the
 276 buoyancy term of the momentum balance (Eq. (4)), where it varies linearly
 277 with temperature and moisture content. The reference temperature is $T_0 =$
 278 $[\max(T_w) + \min(T_w)]/2$. Similarly, the reference concentration of water vapor
 279 is $c_0 = [\max(c_{\text{sat}}(T_w)) + \min(c_{\text{sat}}(T_w))]/2$.

280 3.2. Radiative transfer

281 The radiative power \mathcal{P}_{rad} in the energy balance (Eq. (5)) is defined by

$$\mathcal{P}_{\text{rad}}(\mathbf{r}) = \int_{\nu} \kappa_{\nu} \left(\int_{4\pi} I_{\nu}(\mathbf{r}, \boldsymbol{\Omega}) d\boldsymbol{\Omega} - 4\pi I_{\nu}^{\circ}(T(\mathbf{r})) \right) d\nu, \quad (9)$$

282 where $I_\nu(\mathbf{r}, \boldsymbol{\Omega})$ is the radiative intensity at wavenumber ν , position \mathbf{r} , and
 283 direction $\boldsymbol{\Omega}$, $d\boldsymbol{\Omega}$ is the differential solid angle and $I_\nu^\circ(T(\mathbf{r}))$ is the Planck
 284 equilibrium intensity (blackbody intensity) at temperature T . The absorp-
 285 tion coefficient κ_ν is assumed to be uniform.

286 The radiative intensity satisfies the radiative transfer equation

$$\boldsymbol{\Omega} \cdot \nabla I_\nu(\mathbf{r}, \boldsymbol{\Omega}) = \kappa_\nu (I_\nu^\circ(T(\mathbf{r})) - I_\nu(\mathbf{r}, \boldsymbol{\Omega})). \quad (10)$$

287 Cave walls are assumed to be black (the emissivities of limestone and water
 288 are respectively equal to 0.95 and 0.96 [39], thus close to 1 in both cases).
 289 Therefore, the boundary condition for Eq. (10) at wall positions \mathbf{r}^b for the
 290 propagation directions $\boldsymbol{\Omega}$ such that $\boldsymbol{\Omega} \cdot \mathbf{n} > 0$, \mathbf{n} being the unit vector
 291 normal to the wall pointing to the interior of the domain, writes $I_\nu(\mathbf{r}^b, \boldsymbol{\Omega}) =$
 292 $I_\nu^\circ(T(\mathbf{r}^b))$.

293 The annual variations of gas temperature and water vapor molar fraction
 294 are not large enough to significantly affect the radiative properties of the
 295 mixture. Indeed, the amplitude of temperature fluctuations during the year
 296 is approximately ± 1 K. Assuming saturated water vapor, the corresponding
 297 annual fluctuation of x_w is smaller than $\pm 7\%$. These fluctuations of temper-
 298 ature and water vapor concentration result in variations of the absorption
 299 coefficient κ_ν lower than 7%. The constant absorption spectrum displayed
 300 in Fig. 3 was thus used in all simulations.

301 3.3. Heat and mass fluxes through the cave wall

302 The distribution of the evaporation and heat fluxes through the cave
 303 wall are among the most important outputs of the model. The evaporation
 304 velocity (i.e., the volume of evaporated liquid water per unit of surface and
 305 time) reads:

$$v_{ev} = -\frac{D}{\rho_w} \nabla c \cdot \mathbf{n}, \quad (11)$$

306 where ρ_w is the density of liquid water. v_{ev} is positive for evaporation and
 307 negative for condensation (the normal vector \mathbf{n} is directed towards the cav-
 308 ity).

309 The total heat flux q_{th} through the cave wall is the sum of the conduction
 310 flux q_{con} , the latent heat flux q_{lat} and the radiative flux q_{rad} :

$$q_{th} = \underbrace{-\lambda \nabla T \cdot \mathbf{n}}_{q_{con}} + \underbrace{\mathcal{L} \rho_w v_{ev}}_{q_{lat}} + \underbrace{\int_\nu \int_{4\pi} I_\nu(\mathbf{r}^b, \boldsymbol{\Omega}) \boldsymbol{\Omega} \cdot \mathbf{n} d\boldsymbol{\Omega} d\nu}_{q_{rad}}, \quad (12)$$

Physical property	Name	Numerical value
Air density	ρ_0	1.23 kg.m^{-3}
Kinematic diffusivity	ν	$1.46 \times 10^{-5} \text{ m}^2.\text{s}^{-1}$
Specific heat	C_p	$1.005 \times 10^3 \text{ J.kg}^{-1}.\text{K}^{-1}$
Thermal conductivity	λ	$0.025 \text{ W.m}^{-1}.\text{K}^{-1}$
Thermal diffusivity	α	$2.05 \times 10^{-5} \text{ m}^2.\text{s}^{-1}$
Water latent heat of vaporization	\mathcal{L}	$2.473 \times 10^6 \text{ J.kg}^{-1}$
Thermal expansion coefficient	β_T	$3.51 \times 10^{-3} \text{ K}^{-1}$
Solutal expansion coefficient	β_c	$0.490 \text{ m}^3.\text{kg}^{-1}$
Saturated vapor concentration	$c_{sat}(T_m)$	$1.065 \times 10^{-2} \text{ kg.m}^{-3}$
Derivative of $c_{sat}(T)$	$\beta = c'_{sat}(T_m)$	$7.03 \times 10^{-4} \text{ kg.m}^{-3}.\text{K}^{-1}$
Water/vapor solutal diffusivity	D	$2.43 \times 10^{-5} \text{ m}^2.\text{s}^{-1}$
Prandtl number	$\text{Pr} = \nu/\alpha$	0.712
Schmidt number	$\text{Sc} = \nu/D$	0.601
Lewis number	$\text{Le} = \alpha/D$	0.844

Table 1: Physical properties of the cave atmosphere at temperature $T_m = 285.15 \text{ K} \simeq 12^\circ \text{C}$ (from ref. [22]).

311 where $I_\nu(\mathbf{r}^b, \mathbf{\Omega})$ is the radiative intensity at the cave wall. Equation (12)
312 allows to estimate the relative contribution of each heat transfer mechanism
313 to the total heat flux through the cave wall.

314 4. Numerical methods

315 4.1. Natural convection

316 Flow equations (3)-(6) are solved using a Chebyshev collocation method [40].
317 Domain decomposition along the horizontal direction is carried out by the
318 Schur complement method to make the computations parallel [41]. Time
319 integration is performed through a second-order semi-implicit scheme. The
320 velocity divergence-free condition is enforced using a projection method.

321 The large-eddy simulation (LES) approach is used in this study to save
322 computational time. The Spectral Vanishing Viscosity (SVV) method [42, 43,
323 44] is employed to model the effects of the unresolved subgrid scales, because
324 it is particularly suitable for spectral methods. It consists in introducing an
325 artificial dissipation term to ensure spectral convergence and dissipate the
326 high modes of the Chebyshev polynomial development. The SVV method is

327 implemented in the form of a modified Laplacian operator ∇_{SVV}^2 combining
 328 viscous and SVV dissipation such that

$$\nabla_{SVV}^2 = \nabla \cdot (1 + \nu^{-1}Q)\nabla, \quad (13)$$

329 for the momentum balance. For the energy balance and the water vapor
 330 balance, the same operator is used with the thermal diffusivity α and the
 331 mass diffusivity D instead of the kinematic viscosity ν in Eq. (13). The
 332 viscosity kernel Q acts on each spatial direction independently. In spectral
 333 space, it is given for the i^{th} direction by $\hat{Q}_i(k) = \epsilon_i e^{-\left(\frac{k-N_i}{k-M_i}\right)^2}$, if $k > M_i$
 334 or $\hat{Q}_i(k) = 0$ otherwise, where k is the Chebyshev polynomial order, ϵ_i is
 335 the viscosity amplitude, N_i is the number of collocation point in the i^{th}
 336 direction and $M_i \leq N_i$ is the cut-off spectral mode. ϵ_i and M_i are the
 337 control parameters of the SVV method. The numerical modeling reduces by
 338 either increasing M_i or decreasing ϵ_i . It is worth noting that the same SVV
 339 parameters are used in the momentum balance, in the energy balance and in
 340 the water vapor balance.

341 Simulations have been carried out using a spatial mesh made of $N_x \times$
 342 $N_y \times N_z = 241 \times 241 \times 641$ collocation points. SVV parameters are chosen
 343 such that $M_i = 3N_i/4$ and $\epsilon_i = 1/(4N_i)$ for each spatial direction i . Time
 344 integration is performed with a convection time step $\delta t = 0.001 \times t_{\text{ref}}$, where
 345 $t_{\text{ref}} \simeq 15 \text{ s}$ is the reference time associated with the reference length L_X and
 346 the reference velocity $\sqrt{g\beta_T\Delta TL_X/Pr}$. In Sec. 5, results will be analyzed in
 347 terms of time-averaged quantities over a time period $\Delta t = 100 \times t_{\text{ref}}$, taken
 348 once the statistically steady state is reached.

349 4.2. Radiative transfer

350 The high resolution spectrum of the absorption coefficient displayed in
 351 Fig. 3 contains thousands of spectral lines which makes expensive the com-
 352 putation of the integral over the wavenumbers in Eq. (9). Therefore, we use
 353 the Absorption Distribution Function (ADF) model [45] which consists in
 354 substituting the integration over the wavenumber with an integration over
 355 the values of the absorption coefficient, for which a coarse logarithmic dis-
 356 cretization is sufficient. In the present study, the values of the absorption
 357 coefficient of Fig. 3 have been logarithmically discretized in 16 classes. The
 358 accuracy of this method has been shown to be better than 1 % [46].

359 The radiative transfer equation (10) is solved using a ray-tracing algo-
 360 rithm for each ADF class of absorption coefficient value. The computation

361 is made parallel by distributing the rays among the different processors. The
362 4π angular domain is uniformly discretized using 900 rays from volume cell
363 centers and 450 rays from boundary cell centers. The radiation mesh is
364 coarsened by a factor of five in each direction of space compared with the
365 convection mesh and we use a radiation subgrid model [47] to account for the
366 radiation of the spatial scales resolved by the flow mesh but filtered by the
367 coarse radiation mesh. The radiation of spatial scales unresolved by the flow
368 mesh is ignored. This subgrid model has been validated in various configura-
369 tions and its accuracy is approximately a few per cent on radiative power and
370 wall fluxes. It has been used for the simulation of coupled natural convec-
371 tion and radiation in differentially heated cavities [31] and Rayleigh-Bénard
372 cells [48].

373 Finally, an explicit coupling is carried out between flow and radiation cal-
374 culations and the radiative power is updated every 10 convection time steps
375 δt . Indeed, the flow time step is imposed by numerical stability constraints
376 and does not correspond to significant variations of the temperature field.

377 4.3. Validation

378 We first compare in this section Direct Numerical Simulations (DNS) to
379 some experimental data available in the literature. We then validate the
380 LES approach through comparisons with DNS results in the shallow cave
381 configuration.

382 Figure 5 shows comparisons between DNS and experimental data for
383 Rayleigh-Bénard convection in cubical cavities. The DNS data correspond
384 to isothermal horizontal walls, adiabatic side-walls, dry and non-radiating
385 air. The data were obtained with the same code and numerical setup used in
386 the present study, and were already presented in Ref. [27]. Both experiments
387 and numerical simulations are related to gases with a Prandtl number close
388 to 0.7. In the experiment carried out by Belmonte *et al* [56], the cubical
389 convection cell was put under pressure inside a cylindrical external vessel.
390 The volume between both cavities was filled by cotton batting in order to
391 impede any external motion and to increase thermal insulation of the cavity
392 lateral side-walls. The authors have measured the Nusselt number at the
393 center of the horizontal isothermal plates but they concluded that this value
394 is representative of the average Nusselt number on the surface of the plate.
395 On the opposite, Leong *et al* [57] have considered highly conducting side
396 lateral walls, leading to less uncertain boundary conditions with a nearly
397 linear temperature profile along the vertical axis for these side-walls. The

398 comparisons presented in Fig. 5 show a good agreement between numerical
 399 results and experimental data, despite the differences in side-wall boundary
 400 conditions.

401 In addition, Leong *et al* [57] carried out experiments with differentially
 402 heated cubical cavities, i.e. two vertical and opposite active walls with con-
 403 ducting walls for the four remaining side-walls. They provided a correlation
 404 for this case in the form $Nu = 0.08461 Ra^{0.3125}$ for $10^4 \leq Ra \leq 10^8$. DNS
 405 with the same boundary conditions on the side-walls led to $Nu = 35.73$ at
 406 $Ra = 3 \times 10^8$ [58]. A slight extrapolation of the experimental correlation
 407 yields $Nu = 37.72$, which is in quite satisfactory agreement.

408 In a second step, the Spectral Vanishing Viscosity (SVV) model has been
 409 validated against DNS data in the case of a dry and transparent gas (C case
 410 in Table 3) for the month of February. Table 2 reports LES and DNS re-
 411 sults for macroscopic quantities such as the volume-averaged reduced mean
 412 temperature ($\theta = (T - T_0)/\Delta T$), the volume-averaged dimensionless kinetic
 413 energy of the mean flow, the volume-averaged dimensionless turbulent ki-
 414 netic energy, and the Nusselt number $\overline{Nu} = \overline{q}_{con} L_X / (\lambda \Delta T)$ where \overline{q}_{con} is
 415 the conduction flux averaged at the upper ($X = L_X$), left ($Z = 0$) or side
 416 ($Y = 0$) walls. Two meshes (LES₂₄₀ using $241 \times 241 \times 641$ points and LES₁₆₀
 417 using $161 \times 161 \times 641$ points) and two sets of SVV parameters M and ϵ
 418 are considered to assess the sensitivity of the LES results. The DNS mesh is
 419 made of $321 \times 321 \times 1025$ points. The best agreement is obtained for the LES
 420 parameters retained for the coupled simulations (LES₂₄₀ mesh, $M = 3N/4$,
 421 $\epsilon = 1/(4N)$) with differences with DNS results below 10 %. This maximum
 422 difference is observed for the turbulent kinetic energy. The accuracy of the
 423 LES decreases with the coarser LES₁₆₀ mesh (differences with DNS up to
 424 20 %) but is little affected by the change in SVV parameters M and ϵ . More
 425 details on this validation can be found in Ref. [24].

426 5. Flow field analysis

427 5.1. The studied configurations

428 In order to highlight specific effects associated with gas radiation and so-
 429 lital buoyancy, numerical simulations were performed with different versions
 430 of the model described in Sec. 3. We considered three cases, labelled C, CR
 431 and CRM (see Tab. 3). The CRM model is the full model used as a reference.
 432 It includes gas radiation and the contribution of the water vapor concentra-
 433 tion field to buoyancy. In the CR model, the contribution of the water vapor

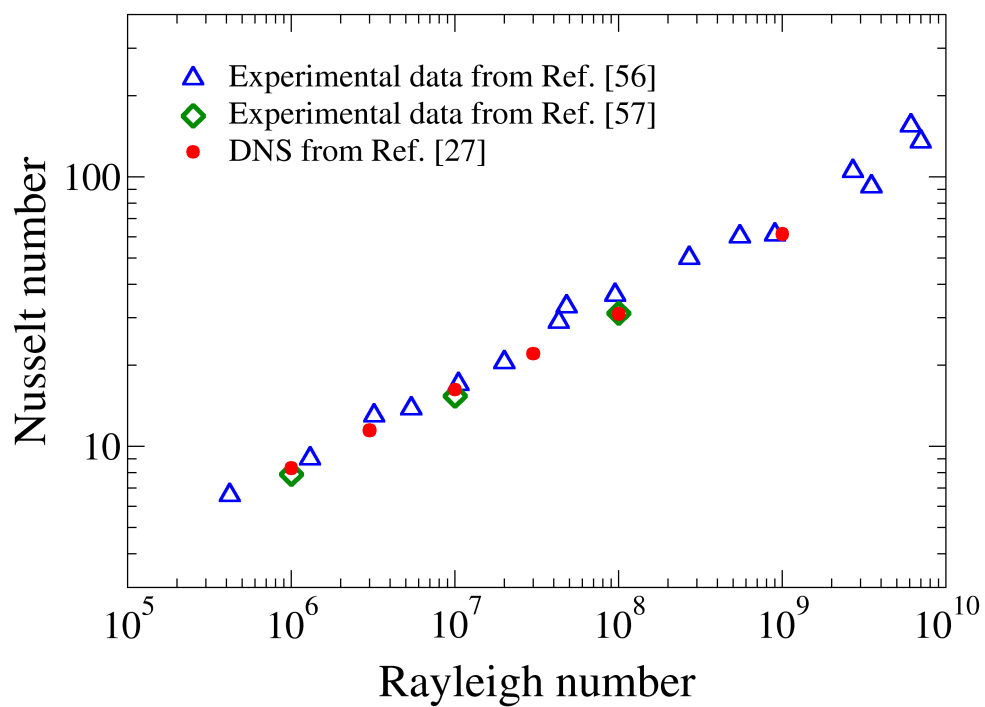


Figure 5: Comparisons between DNS results and experimental data in the case of Rayleigh-Bénard convection in cubical cavities filled with gases. The experimental data are from Belmonte et al [56] with nearly insulated side-walls, and from Leong et al [57] with conducting side-walls. The DNS data correspond to perfectly insulated side-walls [27].

Mesh	M	ϵ	$\theta \times 10^2$	$k_{kin}^* \times 10^4$	$k_{tur}^* \times 10^4$	Nu_{up}	Nu_{left}	Nu_{sides}
DNS	N	0	5.760	2.540	2.710	-14.755	4.968	6.825
LES ₂₄₀	$3N/4$	$1/(4N)$	5.610	2.638	2.998	-15.605	5.381	6.961
LES ₁₆₀	$3N/4$	$1/(4N)$	5.350	2.803	2.547	-16.385	5.979	7.219
LES ₁₆₀	$N/2$	$1/(2N)$	5.370	2.865	2.368	-16.385	6.046	7.192

Table 2: Comparison between LES and DNS results (C case in Table 3, February) on the volume-averaged reduced temperature, the volume-averaged dimensionless kinetic energy of mean flow, the volume-averaged dimensionless turbulent kinetic energy and the averaged Nusselt number at the upper ($X = L_X$), left ($Z = 0$) and side ($Y = 0$) walls.

Case	radiation model	solutal buoyancy
CRM	radiating gas (κ_ν from Fig. 3)	considered (β_c from Tab. 1).
CR	radiating gas (κ_ν from Fig. 3)	disregarded ($\beta_c = 0$)
C	transparent gas ($\kappa_\nu = 0$)	disregarded ($\beta_c = 0$)

Table 3: Three considered cases with different levels of simplifications. The CRM model is the full model described in Sec. 3.

434 field to buoyancy is ignored ($\beta_c = 0$), so that the velocity and temperature
435 fields can be computed without solving the mass conservation equation (6).
436 The C model uses the same simplifying assumption for buoyancy. In addition,
437 the gas is assumed to be transparent ($\kappa_\nu = 0$). The radiative power is
438 thus zero ($\mathcal{P}_{rad} = 0$), and the radiative transfer equation (10) can be removed
439 from the model. The convection–radiation coupling is thus ignored in model
440 C, but radiative fluxes still exist between the cave walls separated by the
441 transparent atmosphere. This is the model already used in Ref. [24].

442 5.2. Flow pattern

443 Figure 6 shows streamlines of the mean velocity field colored by the ki-
444 netic energy of the mean flow in the Y mid-plane for the three models listed in
445 Tab. 3. In the C case, flow patterns and convection intensities differ consid-
446 erably between May and November, as discussed in previous work [24]. The
447 maximum and minimum wall temperatures are the same for both months,
448 but the mean vertical temperature gradient is negative (i.e., unstable) in May
449 and positive (i.e., stable) in November (see Fig.2). This leads to a one-cell
450 flow pattern associated with intense convection in May and a multiple-cell
451 flow pattern associated with weaker convection in November.

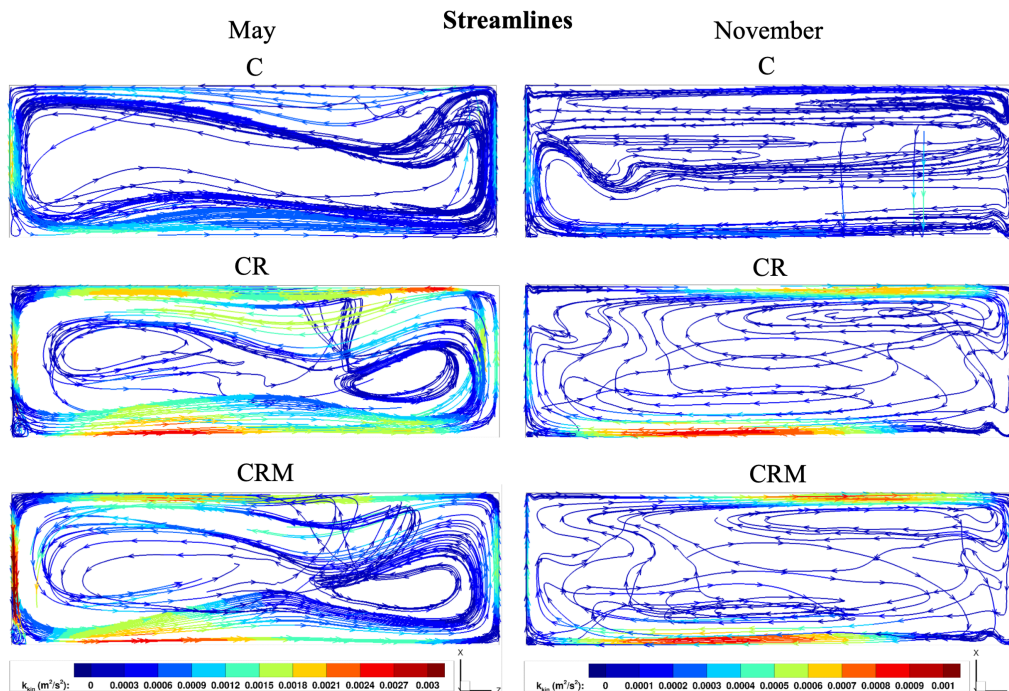


Figure 6: Flow streamlines colored by the kinetic energy of the mean flow for May (left column) and November (right column), for the models C, CR and CRM (see table 3). Streamlines are drawn from the Y mid-plane and then projected onto the Y mid-plane when they deviate from it.

452 Comparing CR and CRM models for both months, we observe that flow
 453 patterns are very similar. This suggests that the solutal buoyancy effect
 454 on the flow behavior might be insignificant. Conversely, the gas radiation
 455 increases the flow circulation and modifies the streamlines of the mean flow.
 456 In May, two secondary cells are observed in the core when the gas radiation
 457 is taken into account (CR and CRM cases). In November, gas radiation
 458 unsettle the multiple-cell flow pattern observed in case C. Indeed, the flow
 459 pattern observed in cases CR and CRM is closer to a one-cell large-scale
 460 circulation due to increased kinetic energy of the mean flow, even if two
 461 weak secondary cells are noticeable in the upper right and lower regions.

462 In order to quantify the previous observations, the following macroscopic
 463 quantities are reported in Tab. 4: the volume-averaged kinetic energy of the
 464 mean flow $k_{kin} = \langle \frac{1}{2} \bar{\mathbf{u}} \cdot \bar{\mathbf{u}} \rangle_V$, the volume-averaged turbulent kinetic energy
 465 $k_{tur} = \langle \frac{1}{2} \mathbf{u}' \cdot \mathbf{u}' \rangle_V$ and the maximum of the mean vertical velocity $|\bar{u}|_{\max}$,

May			
	C	CR	CRM
$k_{kin} \times 10^4 \text{ (m}^2/\text{s}^2)$	2.8	6.8	6.9
$k_{tur} \times 10^4 \text{ (m}^2/\text{s}^2)$	0.93	2.7	3.2
$ \bar{u} _{\max} \text{ (m/s)}$	0.095	0.105	0.108
November			
	C	CR	CRM
$k_{kin} \times 10^4 \text{ (m}^2/\text{s}^2)$	0.31	1.1	1.1
$k_{tur} \times 10^4 \text{ (m}^2/\text{s}^2)$	0.066	0.14	0.14
$ \bar{u} _{\max} \text{ (m/s)}$	0.050	0.069	0.069

Table 4: Macroscopic flow quantities

466 where $\bar{\cdot}$ and $\langle \cdot \rangle_V$ denote time-averaging and volume-averaging, respectively.
467 The comparison between CR and CRM cases confirms the low impact of
468 solutal buoyancy on the flow behavior. Indeed, with the exception of the
469 turbulent kinetic energy k_{kin} which increases by 19 % between CR and CRM
470 models in May, macroscopic quantities are not significantly modified by so-
471 lutal buoyancy. This weak effect of the moisture gradient on the flow pattern
472 can be readily explained by estimating the order of magnitude of the ratio
473 between the solutal and thermal contributions to buoyancy:

$$\frac{g\beta_c(\beta\Delta T)}{g\beta_T\Delta T} = \frac{\beta_c\beta}{\beta_T} \simeq 0.098 \ll 1. \quad (14)$$

474 The solutal contribution is thus negligible compared to the thermal contri-
475 bution.

476 Conversely, the macroscopic quantities in Tab. 4 confirm the thermal
477 convection enhancement due to gas emission and absorption. The kinetic
478 energies k_{kin} and k_{tur} are 2 to 3 times higher in the CR case compared to the
479 C case for both May and November, and $|\bar{u}|_{\max}$ is increased by 11 % in May
480 and by 14 % in November. The gas radiation effect will be discussed in more
481 detail in Sec. 5.3.

482 5.3. Velocity and thermal fields

483 Figure 7 displays horizontal profiles of the vertical velocity component
484 and of the temperature close to the left and right walls in the Y mid-plane,
485 at three different heights X , in May. The results from the three models C,

486 CR and CRM are shown. CR and CRM models yield similar profiles, fur-
 487 ther confirming the weak solutal buoyancy effect on the flow behavior. The
 488 thickness of the fluid layer flowing along the walls is drastically increased
 489 due to the change in the temperature distribution induced by gas-wall ra-
 490 diative exchanges. For this month, the gas flows downward along the cold
 491 left wall and upward along the hot right wall for the three cases C, CR and
 492 CRM (Figs. 7a and 7b). The upward buoyant motion along the right wall is
 493 strengthened by the gas radiation as the fluid is heated outside the thermal
 494 boundary layer due to the absorption of the wall radiation (black curves in
 495 Fig. 7d) resulting in the thickening of the ascending fluid layer. This mecha-
 496 nism of flow enhancement by gas-wall radiative exchanges has been reported
 497 in the literature about the differentially heated cavity. It has been evidenced
 498 both numerically [30, 31, 32, 33] and experimentally [49].

499 A similar effect is observed along the left wall where the fluid is cooled
 500 in the top left corner due to the emission by the gas (red curves in Fig. 7c).
 501 The ascending flow observed at the bottom of this wall (black curves) is due
 502 to the presence of a small vortex in the corner (see Fig. 6). Interestingly
 503 enough, the inner part of the hydrodynamic and thermal boundary layers
 504 (few centimeters thick) is not affected by gas radiation (see Fig. 7). The
 505 same trends were observed in November, although the situation is further
 506 complicated by the change in the flow pattern induced by gas radiation.

507 The horizontal velocity component and the temperature profiles along the
 508 vertical centerline of the cavity ($Z = L_Z/2$ and $Y = L_Y/2$) are displayed in
 509 Fig. 8. As already discussed, the comparison between CRM and CR models
 510 does not show any noticeable effect of the solutal buoyancy. Fig. 8a exhibits
 511 the intensification of the large-scale counter-clockwise circulation due to the
 512 gas radiation effect in May, associated with strong mixing effects resulting
 513 in nearly isothermal temperature field in the cavity core (see Fig. 8b, red
 514 curves) similar to the profile predicted by the C model. The temperature
 515 gradients are confined very close to the walls and are not modified by gas
 516 radiation. In November, the multiple-cell regime predicted by the C model
 517 is broken by the gas radiation effect (see Fig. 6). The horizontal air motion
 518 becomes stronger near the horizontal walls but a part of the core remains
 519 almost motionless. We observe a little effect of gas radiation on the vertical
 520 temperature profiles (see Fig. 8b, blue curves) but this effect is too weak to
 521 significantly modify the thermal stratification obtained with the C model.

522 Figure 9 presents the vapor concentration profile along the vertical cen-
 523 terline of the cavity. Due to the analogy between heat and mass transfer,

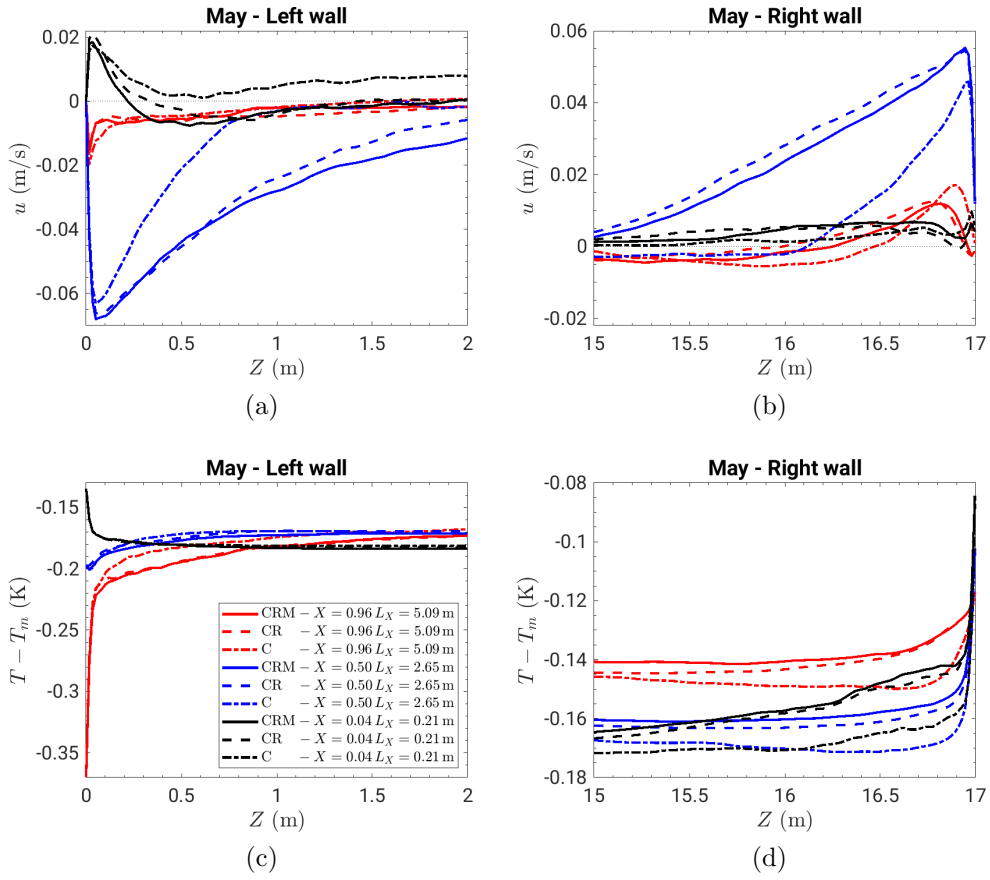


Figure 7: Horizontal profiles of the vertical velocity component u (a) and (b), and of the temperature (c) and (d), in the Y mid-plane at different heights X along the vertical walls for C, CR and CRM models, in May.

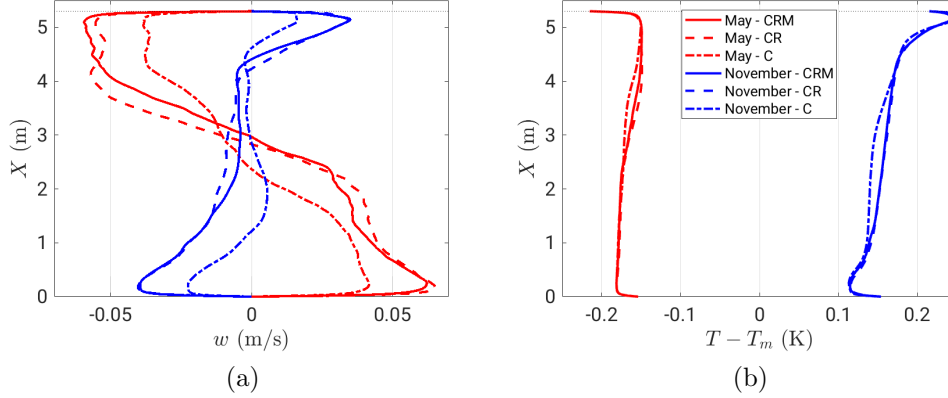


Figure 8: Vertical profiles of the horizontal velocity component W (a) and the temperature (b) along the vertical centerline of the cavity ($Z = L_Z/2$ and $Y = L_Y/2$) for the C, CR and CRM models in May (red curves) and November (blue curves).

524 the solutal and thermal stratifications are quite similar. However, there is a
 525 local non-monotonic variation of the concentration vertical profile in Novem-
 526 ber not observed on the corresponding temperature profile. Because of the
 527 homogenization by gas-gas radiative exchanges, the temperature profile is
 528 likely less sensitive to the presence of small secondary cells predicted by the
 529 CRM model in the core of the cavity in November.

530 6. Heat and mass transfer through the cavity wall

531 6.1. Effect of gas radiation on the conductive and radiative fluxes

532 Figure 10 shows the spatial distribution of the conductive and radiative
 533 fluxes along the cavity walls at the mid-plane $Y = L_Y/2$. We checked that
 534 CR and CRM models gave indistinguishable results because of the negligi-
 535 ble effect of solutal buoyancy (not shown). Differences between the results
 536 from C and CRM models is thus due to the presence of gas radiation in the
 537 latter case. Despite the strong convection enhancement associated with gas
 538 radiation (see Sec. 5.2 and 5.3), the conductive fluxes q_{cond} (blue curves in
 539 Fig. 10) are little affected by radiation effects. Gas radiation tends to slightly
 540 decrease the conductive flux, but the effect is hardly significant. This is con-
 541 sistent with the temperature profiles displayed in Fig. 7c, 7d and 8b, showing
 542 that the wall temperature gradient is not affected by gas radiation.

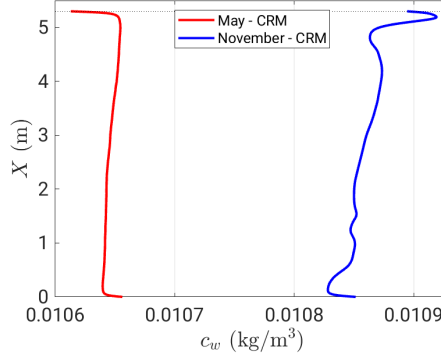


Figure 9: Vapor concentration profile along the vertical centerline of the cavity ($Z = L_Z/2$ and $Y = L_Y/2$) for the CRM model in May and November.

543 On the other hand, Fig. 10 shows that gas radiation significantly modifies
 544 the distribution of the radiative flux q_{rad} along the walls (red curves). The
 545 absolute value of the wall radiative flux is rather decreased by gas radiation
 546 along the top and bottom walls mainly due to a screening effect. For the left
 547 and right walls, the flux is rather increased but the analysis is made difficult
 548 by the complex structure of the temperature field in front of these walls.

549 The effect of gas radiation can go up to a factor two, leaving the order
 550 of magnitude of the wall radiative flux unchanged. This result is consistent
 551 with the value of the transmissivity $\tau_g \simeq 0.7$ found in Sec. 2.3. The cavity of
 552 approximately 10 m length is at the transition between the regimes dominated
 553 by wall-to-wall radiation ($\tau_g \simeq 1$) and gas-wall radiation ($\tau_g \ll 1$). This
 554 behavior would likely be different in a larger cavity, with a characteristic
 555 length of a few tens of meters.

556 6.2. Energy balance at the cavity wall

557 The total heat flux q_{th} through the cave walls can be broken down into
 558 three terms: the conductive flux q_{con} , the radiative flux q_{rad} and the latent
 559 heat flux q_{lat} (see Eq. (12)). In this section, we analyze the relative signifi-
 560 cance of these three contributions in the energy balance.

561 6.2.1. Approximate expressions of the mass and latent heat fluxes in CR and 562 C models

563 Although the solutal contribution to buoyancy is ignored in models C
 564 and CR, solving the mass conservation Eq. (6) with the Dirichlet boundary

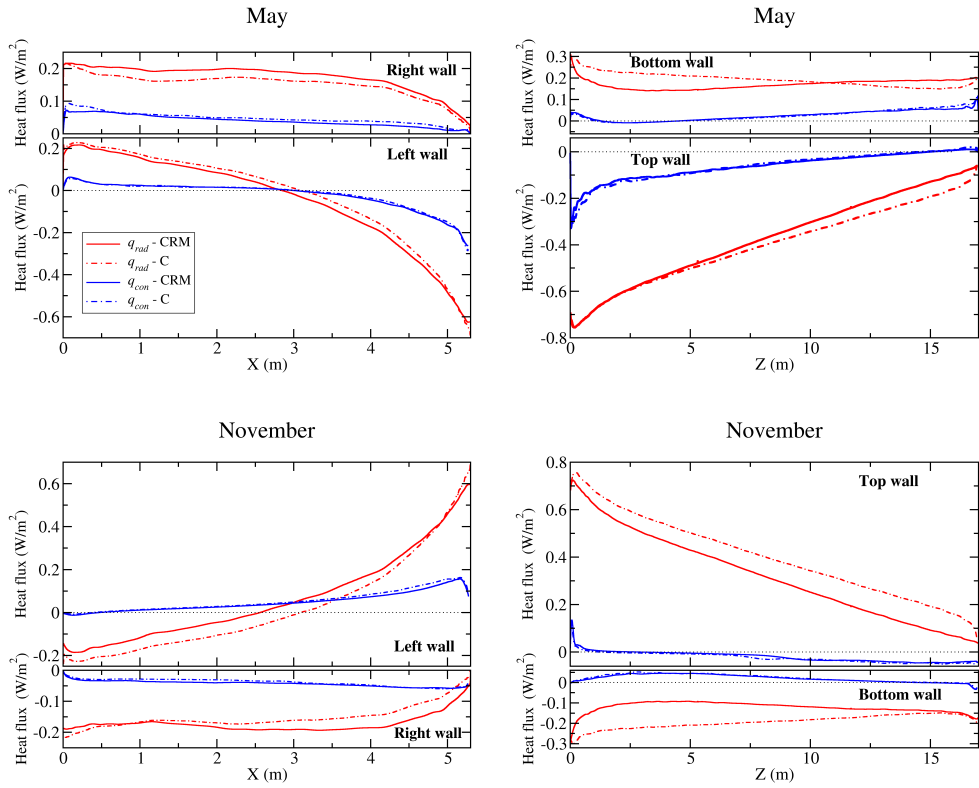


Figure 10: Spatial distribution of conductive (blue lines) and radiative (red lines) heat fluxes at the mid-plane $Y = L_Y/2$ along the left ($Z = 0$), right ($Z = L_Z$), bottom ($X = 0$) and top ($X = L_X$) walls, computed from the CRM and C models in May and November.

565 condition Eq. (7) is required to get the mass flux $\rho_w v_{ev}$ and the latent heat
 566 flux $q_{lat} = \mathcal{L} \rho_w v_{ev}$ through the cavity wall. However, this resolution can be
 567 avoided using an approximate solution based on the analogy between heat
 568 and mass transfer. With the following assumptions:

- 569 1. c_{sat} varies linearly with the gas temperature T ,
- 570 2. the solutal and thermal diffusivities are equal (i.e., $Le = 1$),
- 571 3. the conductive flux through the cavity wall is not modified by gas
 572 radiation,

573 the dimensionless conductive and mass fluxes through the cavity wall, respec-
 574 tively the Nusselt number $Nu = q_{con} L_X / (\lambda \Delta T)$ and the Sherwood number
 575 $Sh = \rho_w v_{ev} L_X / (D \beta \Delta T)$, would be equal. The assumptions 1 and 2 above
 576 are generally valid in caves, because small temperature variations allow the
 577 linearization of $c_{sat}(T)$ and $Le \sim 1$ is a general property of gases. The as-
 578 sumption 3 is expected to be valid in cavities where radiative transfer is not
 579 dominated by gas radiation, i.e., cavities for which the relation $\tau_g \sim 1$
 580 is satisfied. For the specific cavity studied in this work, the assumption 3 has
 581 been evidenced in Sec. 6.1, and the relation $Nu \simeq Sh$ is confirmed in Fig. 11.
 582 It yields:

$$\rho_w v_{ev} = \left(\frac{D \beta}{\lambda} \right) q_{con} \quad \text{and} \quad q_{lat} = \left(\mathcal{L} \frac{D \beta}{\lambda} \right) q_{con} \simeq 1.7 q_{con}. \quad (15)$$

583 These relations allow to compute the mass flux $\rho_w v_{ev}$ and the latent heat
 584 flux q_{lat} from the conductive flux q_{con} and the physical properties of the cave
 585 atmosphere. They have been already used by Dreybrodt and Gabrovšek [11]
 586 to assess the order of magnitude of condensation fluxes in caves through
 587 simple models.

588 6.2.2. *Relative contribution of conductive, radiative and latent heat fluxes to* 589 *the total flux*

590 We showed in a previous work that conduction was mainly dominated
 591 by radiative fluxes between the walls of the cavity filled with a dry and
 592 transparent atmosphere [24]. This remains true for the wet and radiant
 593 atmosphere considered in this work because: (1) the solutal buoyancy has a
 594 negligible effect on the flow, (2) gas radiation hardly changes the conductive
 595 flux and does not modify the order of magnitude of the radiative flux (see
 596 Sec. 6.1). Indeed, one can check in Fig. 10 that, with the exception of limited

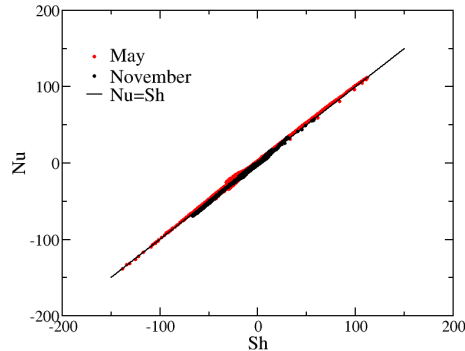


Figure 11: Cloud of points representing the local Nusselt number versus the local Sherwood number for May and November for the CRM model. Each point corresponds to a given spatial location on the wall.

597 areas where both q_{rad} and q_{con} go to zero, $|q_{rad}/q_{con}| \gtrsim 1$ over the whole cavity
 598 surface. More precisely, $1 \lesssim |q_{rad}/q_{con}| \lesssim 3$ in May at the upper left edge
 599 (intersection of top and left walls) or at the right of the bottom wall, and in
 600 November at the upper right edge (intersection of the top and right walls)
 601 and on a part of the bottom wall. $|q_{rad}/q_{con}| \gtrsim 3$ everywhere else.

602 The latent heat flux q_{lat} must also be considered in the energy balance.
 603 Eq. (15) yields $(q_{con} + q_{lat}) \simeq 2.7 q_{con}$. The added conduction and phase
 604 change contributions, both driven by convection, are comparable with the ra-
 605 diation contribution in many places on the walls, and dominate heat transfer
 606 in the areas such that $|q_{rad}/q_{con}| \lesssim 3$. The full spatial distribution of the total
 607 heat flux q_{th} and its components q_{con} , q_{lat} and q_{rad} are shown in Fig. 12 for
 608 the CRM model in May. It is noteworthy that the contribution of convection
 609 ($q_{con} + q_{lat}$) is comparable to that of radiation at the upper left edge, where
 610 the heat transfer is most intense. The same remark applies in November (not
 611 shown).

612 The wall temperature used in boundary conditions (Eq. (7)) were deter-
 613 mined by a large scale model including heat conduction in the rock mass.
 614 In this model, the contribution of convection to the energy balance at the
 615 cavity walls was assumed negligible with respect to radiation. We see that
 616 this assumption fails when humid air is considered. With the addition of the
 617 conduction and latent heat fluxes, convection significantly contributes to the
 618 heat transfer at the walls. In the configuration studied here, the convection
 619 contribution does not exceed radiation, so that the orders of magnitude of

620 the fluxes should be correctly predicted. However, a full coupling between
 621 conduction in the rock and convection inside the cavity should be considered
 622 to get an accurate solution in the case of humid air. The feasibility of such
 623 simulations will be discussed in the conclusion.

624 *6.3. Mass flux through the cavity wall and consequences on corrosion*

625 As stated in the introduction, condensation and evaporation are of pri-
 626 mary interest for the conservation of painted caves. Condensation results
 627 in wall corrosion by limestone dissolution. Conversely, evaporation induces
 628 limestone deposition. The retreat velocity of the wall v_{ret} is defined as the
 629 volume of dissolved limestone per unit of surface and time ($v_{ret} < 0$ indicates
 630 limestone deposition).

631 The evaporation velocity fields on the cave walls are displayed in Fig. 13
 632 for May and November. In May, condensation takes place on the upper
 633 left walls, over 43 % of the cavity surface. The maximum condensation
 634 rate reaches $18 \mu\text{m}/\text{day}$ at the upper left edge, where the distance from the
 635 ground surface is the shortest (see Fig. 1). The evaporation rate culminates
 636 at $6 \mu\text{m}/\text{day}$ at the lower right edge. The situation is reversed in November.
 637 In this case, evaporation takes place on the upper left walls over 41 % of the
 638 cavity surface. The maximum rate is $9 \mu\text{m}/\text{day}$. Condensation is observed on
 639 the lower right walls, with a maximum rate of $3 \mu\text{m}/\text{day}$. In May, the negative
 640 (unstable) vertical temperature gradient enhances convection, resulting in
 641 maximum condensation or evaporation rates multiplied by two compared to
 642 November, which is associated with positive (stable) vertical temperature
 643 gradient. Therefore, during a full year, there will be more condensation than
 644 evaporation in the upper left part of the cave, and the opposite in the lower
 645 right part.

646 The retreat velocity of the wall can be easily deduced from the evaporation
 647 velocity. The dissolution of 1 mol of CaCO_3 yields 1 mol of ions Ca^{2+} in
 648 solution. The concentration of ions Ca^{2+} in a water solution in equilibrium
 649 with CaCO_3 and a gas phase including CO_2 at partial pressure P_{CO_2} is given
 650 by

$$[\text{Ca}^{2+}] \simeq \mathcal{K} P_{\text{CO}_2}^{1/3} \quad (16)$$

651 where the parameter \mathcal{K} can be computed from the equilibrium constants of
 652 the system $\text{H}_2\text{O}/\text{CO}_2/\text{CaCO}_3$ [50]. Using the data from Ref. [51], we get
 653 $\mathcal{K} \simeq 8.27 \text{ mmol.L}^{-1}.\text{atm}^{-1/3}$ at 12°C (CaCO_3 in calcite form). Dreybrodt
 654 and Gabrovšek [11] showed that the thin film of condensed water lying on a

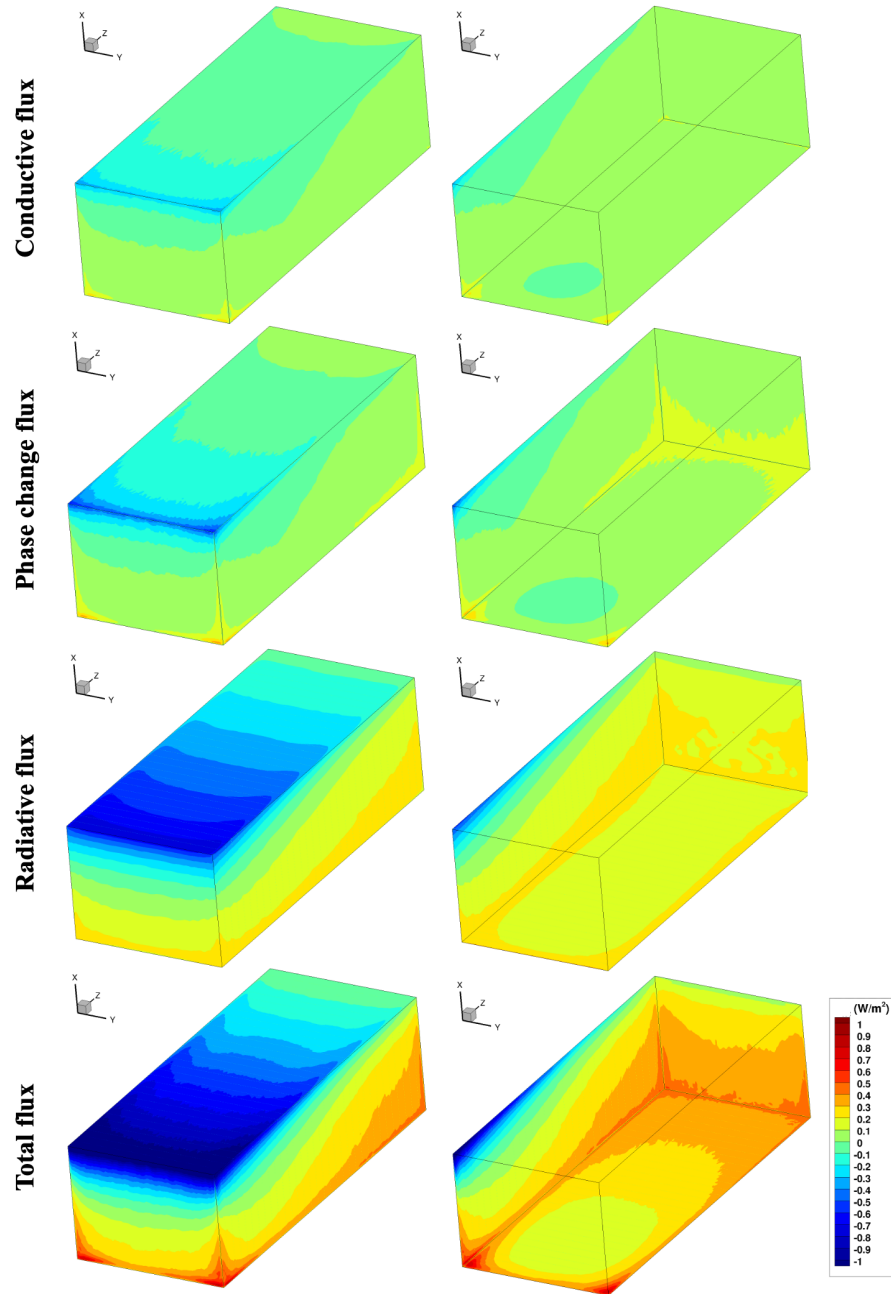


Figure 12: Spatial distribution of conductive (q_{con}), water phase change (q_{lat}), radiative (q_{rad}) and total (q_{th}) wall heat fluxes for the CRM model in May. The left panel corresponds to the top ($X = L_X$), left ($Z = 0$) and front ($Y = L_Y$) cave walls. The right panel corresponds to the bottom ($X = 0$), right ($Z = L_Z$) and rear ($Y = 0$) cave walls.

655 limestone wall can be regarded as saturated with respect to limestone and
 656 CO₂. They came to this conclusion after performing a series of laboratory
 657 experiments covering wide ranges of condensation rates and CO₂ partial pres-
 658 sure commonly found in nature. The retreat velocity can thus be deduced
 659 from Eq. (16) along with mass conservation:

$$v_{ret} = -\frac{\mathcal{K}\mathcal{M}}{\rho_c} P_{CO_2}^{1/3} v_{ev} \quad (17)$$

660 where $\mathcal{M} \simeq 100$ g/mol and $\rho_c \simeq 2700$ kg/m³ are the molar mass and the
 661 density of CaCO₃, respectively. The value $P_{CO_2} = x_{CO_2} P_{atm} = 0.02$ atm is
 662 considered in the following.

663 The behavior of the retreat velocity v_{ret} can be directly deduced from
 664 the evaporation velocity v_{ev} , since both velocities are proportional. The
 665 upper left edge undergoes corrosion in May and deposition in November,
 666 with retreat velocities reaching respectively 0.55 and -0.27 μ m/year. Con-
 667 versely, the lower right edge undergoes evaporation in May and condensation
 668 in November, with retreat velocities of -0.18 and 0.09 μ m/year, respectively.
 669 Therefore, over a full year, dissolution dominates in the upper left region,
 670 and deposition in the lower right region.

671 There are few studies in the literature providing quantitative measure-
 672 ments of condensation or evaporation rates in caves. In the Glowworm cave
 673 (New Zealand), when the cave entrance was closed to prevent air circula-
 674 tion, De Freitas and Schmekal [52] measured condensation and evaporation
 675 rates oscillating from 0 to approximately 10 μ m/day. Buecher [53] measured
 676 evaporation rates in Kartchen Caverns (Arizona), a wet cave with water per-
 677 colating from the surface, little air exchange with the outside, and thus high
 678 relative humidity (over 99%). The average evaporation rate for all stations
 679 installed in the cave was 10 μ m/day, reduced to 6 μ m/day for stations far
 680 from the entrance. The orders of magnitude predicted by our numerical sim-
 681 ulations (a few microns per day) are in line with these values. Condensation
 682 rates higher by an order of magnitude were reported in the literature (see
 683 Ref. [54]), but in configurations far from the one studied in this article (high-
 684 ventilated areas or hydrothermal caves). Corrosion induced by condensation
 685 was also investigated. Cailhol *et al* [55] found from a literature review that
 686 the retreat velocity in a limestone cave should be in the range from 0.3 to
 687 30 μ m/year. Our estimation for a weakly ventilated cave (a few tenths of a
 688 micron per year) falls in the lower part of this range.

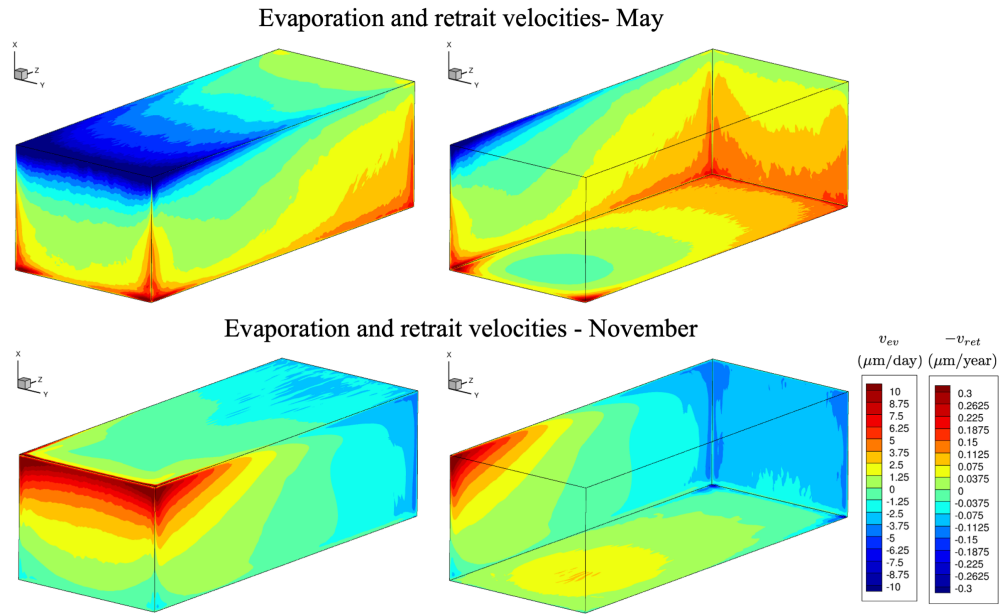


Figure 13: Spatial distribution of the evaporation velocity v_{ev} and the retreat velocity v_{ret} from the CRM model in May and November. v_{ret} is proportional to v_{ev} [from Eq.(17): $v_{ret}/(\mu\text{m}/\text{year}) \simeq -0.030 v_{ev}/(\mu\text{m}/\text{day})$]. The left panel corresponds to the top ($X = L_X$), left ($Z = 0$) and front ($Y = L_Y$) cave walls. The right panel corresponds to the bottom ($X = 0$), right ($Z = L_Z$) and rear ($Y = 0$) cave walls.

689 **7. Conclusion**

690 A major outcome of the numerical simulations is the strong similarities
691 between the results obtained in the shallow cave considered in this study and
692 in the classical differentially heated cavity, despite the simplicity of the ther-
693 mal boundary conditions in the latter case (two isothermal vertical parallel
694 walls surrounded by adiabatic walls). In a shallow cave, opposite vertical and
695 horizontal walls at different distances from the ground surface have different
696 non-uniform temperatures. Due to buoyancy forces, the hot and cold ver-
697 tical walls classically drive the air flow upward and downward, respectively,
698 inducing a global circulation in the cavity. Convection is enhanced when the
699 vertical temperature gradient is negative, i.e., when the floor is warmer than
700 the ceiling.

701 Heat and mass fluxes are maximum in areas of the cavity roof where the
702 distance from the ground is the shortest. Due to the asymmetry induced by
703 the inversion of the vertical temperature gradient twice a year, net conden-
704 sation/corrosion is expected in these areas, whereas the other regions of the
705 cave undergo net evaporation/deposition. The orders of magnitude of the
706 condensation flux (a few microns per day) and of the retreat velocity (a few
707 tenth of a micron per year) are in line with the field data available in the
708 literature.

709 Gas radiation increases the flow circulation in the cavity through wall-
710 gas radiative exchanges. This results in a higher stirring of the cavity core,
711 but the wall conduction and mass fluxes are not modified. This effect was
712 already observed in the differentially heated cavity. In contrast, gas radiation
713 significantly modifies the wall radiative flux, but without changing its order
714 of magnitude. This is consistent with the estimation of the transmissivity
715 ($\tau_g \simeq 0.7$) based on the cavity size (approximately 10 m). A transmissivity
716 slightly lower than 1 indicates a transition between the regimes dominated by
717 surface radiation and gas radiation. Gas radiation should be clearly dominant
718 for larger cavities (typically a few tens of meters).

719 The contribution of the water concentration gradient to buoyancy can be
720 neglected compared to the temperature contribution. However, the heat flux
721 released by the latent heat of evaporation or condensation must be considered
722 in the energy balance at the wall. Indeed, the addition of the latent heat and
723 conduction fluxes, both driven by convection, prevails over radiation in some
724 regions of the cavity. Therefore, more accurate predictions of heat and mass
725 fluxes at the cavity walls require to couple natural convection inside the

726 cavity with conduction in the rock mass. Although the present Large-Eddy
727 Simulations are computationally expensive, this coupling should be feasible
728 given the large time scale associated with the conduction in the rock allowing
729 low coupling frequencies. A last limitation of this study is the cave geometry
730 that is not representative of actual caves. Considering realistic geometries
731 and unstructured meshes would increase the computational time required for
732 the flow simulation but associated numerical methods (finite element, finite-
733 volume) would benefit from a much more efficient parallel implementation
734 than our spectral algorithm.

735 **Acknowledgements**

736 This work was funded by the financial support of the LabeX LaSIPS
737 (ANR-10-LABX-0032-LaSIPS) managed by the French National Research
738 Agency under the "Investissements d'avenir" program (ANR-11-IDEX-0003-
739 02). This work was granted access to the HPC resources of IDRIS under the
740 allocation 2021- A0102B00209 attributed by GENCI (Grand Equipement Na-
741 tional de Calcul Intensif). This work was also performed using HPC resources
742 from the "Mésocentre" computing center of CentraleSupélec and École Nor-
743 male Supérieure Paris-Saclay supported by CNRS and Région Île-de-France
744 (<http://mesocentre.centralesupelec.fr/>).

745 **References**

- 746 [1] M. Cuthbert, G. Rau, M. Andersen, H. Roshan, H. Rutledge, C. Marjo,
747 M. Markowska, C. Jex, P. Graham, G. Mariethoz, R. Acworth, A. Baker,
748 Evaporative cooling of speleothem drip water, *Sci. Rep.* 4 (2014) 5162.
- 749 [2] Y. Lv, Y. Jiang, W. Hu, M. Cao, Y. Mao, A review of the effects of
750 tunnel excavation on the hydrology, ecology, and environment in karst
751 areas: Current status, challenges, and perspectives, *J. Hydrogeol.* 586
752 (2020) 124891.
- 753 [3] D. C. Culver, T. Pipan, *The biology of caves and other subterranean*
754 *habitats*, Oxford University Press, 2009.
- 755 [4] P. L. Fernández, I. Gutierrez, L. S. Quindós, J. Soto, E. Villar, Natural
756 ventilation of the paintings room in the Altamira Cave, *Nature* 321
757 (1986) 586–588.

- 758 [5] A. A. Cigna, Environmental management of tourist caves, *Environ.*
759 *Geol.* 21 (1993) 173–180.
- 760 [6] S. Sánchez-Moral, V. Soler, J. Cañaveras, E. Sanz-Rubio, R. Van
761 Grieken, K. Gysels, Inorganic deterioration affecting the Altamira Cave,
762 N Spain: quantitative approach to wall-corrosion (solutional etching)
763 processes induced by visitors, *Sci. Total Environ.* 243-244 (1999) 67–84.
- 764 [7] J. Brunet, J. Vouvé, P. Malaurent, Re-establishing an underground cli-
765 mate appropriate for the conservation of the prehistoric paintings and
766 engravings at Lascaux, *Conserv. Manage. Archaeol. Sites* 4 (2000) 33–
767 45.
- 768 [8] F. Bourges, P. Genthon, D. Genty, M. Lorblanchet, E. Mauduit,
769 D. D’Hulst, Conservation of prehistoric caves and stability of their in-
770 ner climate: Lessons from Chauvet and other French caves, *Sci. Total*
771 *Environ.* 493 (2014) 79–91.
- 772 [9] P. M. Martin-Sanchez, A. Z. Miller, C. Saiz-Jimenez, Lascaux Cave: An
773 example of fragile ecological balance in subterranean environments, in:
774 E. A. Summers (Ed.), *Microbial life of cave systems*, De Gruyter, 2015,
775 Ch. 13, pp. 279–301.
- 776 [10] R. F. Tarhule-Lips, D. C. Ford, Condensation corrosion in caves on
777 Cayman Brac and Isla des Mona, *J. Cave Karst Studies* 60 (1998) 84–
778 95.
- 779 [11] W. Dreybrodt, F. Gabrovšek, M. Perne, Condensation corrosion: a the-
780 oretical approach, *Acta carsologica* 34 (2005) 317–348.
- 781 [12] P. Malaurent, J. Brunet, D. Lacanette, J.-P. Caltagirone, Contribution
782 of numerical modelling of environmental parameters to the conservation
783 of prehistoric cave paintings: the example of Lascaux Cave, *Conserv.*
784 *Manage. Archaeol. Sites* 8 (2007) 59–76.
- 785 [13] L. Laiz, J. Gonzalez, C. Saiz-Jimenez, Microbial communities in caves:
786 ecology, physiology, and effects on Paleolithic paintings, *Art, biology,*
787 *and conservation: Biodeterioration of works of art* (2003) 210–225.
- 788 [14] Y. Li, D. Ogura, S. Hokoi, J. Wang, T. Ishizaki, Predicting hygrothermal
789 behavior of an underground stone chamber with 3-D modeling to restrain

- 790 water-related damage to mural paintings, *Journal of Asian Architecture*
791 *and Building Engineering* 13 (2014) 499–506.
- 792 [15] J. Martin, F. Doumenc, Condensation–induced self–patterning of a thin
793 clayey layer, *EPL* 138 (2022) 13001.
- 794 [16] A. Bini, M. Cavalli Gori, G. S., A critical review of hypotheses on the
795 origin of vermiculations, *Int. J. Speleol.* 10 (1978) 11–33.
- 796 [17] S. Hoerlé, S. Konik, É. Chalmin, Les vermiculations de la grotte de
797 lascaux : identification de sources de matériaux mobilisables par micro-
798 analyses physico-chimiques, *Karstologia* 58 (2011) 29–40.
- 799 [18] J. Clottes, Midi-Pyrénées, *Gallia Préhistoire* 24 (2) (1981) 525–570.
- 800 [19] L. S. Quindós, A. Bonet, N. Diaz-Caneja, P. L. Fernandez, I. Gutierrez,
801 J. R. Solana, J. Soto, E. Villar, Study of the environmental variables
802 affecting the natural preservation of the Altamira Cave paintings located
803 at Santillana del Mar, Spain, *Atmos. Environ.* 21 (1987) 551–560.
- 804 [20] E. Villar, P. L. Fernández, L. S. Quindós, J. R. Solana, J. Soto, Tem-
805 perature of rock surfaces in Altamira Cave (Spain), *Cave Sci.* 10 (1983)
806 165–170.
- 807 [21] N. Houillon, R. Lastennet, A. Denis, P. Malaurent, S. Minvielle,
808 N. Peyraube, Assessing cave internal aerology in understanding carbon
809 dioxide (CO₂) dynamics: implications on calcite mass variation on the
810 wall of Lascaux Cave (France), *Environ. Earth Sci.* 76 (2017) 170.
- 811 [22] B. Guerrier, F. Doumenc, A. Roux, S. Mergui, P.-Y. Jeannin, Climatol-
812 ogy in shallow caves with negligible ventilation: heat and mass transfer,
813 *Int. J. Therm. Sci.* 146 (2019) 106066.
- 814 [23] N. Houillon, La dynamique du carbone inorganique dans le continuum
815 sol-épikarstique-cavité du site de la grotte de Lascaux (France), Ph.D.
816 thesis, University of Bordeaux (2016).
- 817 [24] B. Qaddah, L. Soucasse, F. Doumenc, S. Mergui, P. Rivière, A. Soufiani,
818 Influence of turbulent natural convection on heat transfer in shallow
819 caves, *Int. J. Therm. Sci.* 177 (2022) 107524.

- 820 [25] P.-Y. Jeannin, M. Hessenauer, A. Malard, V. Chapuis, Impact of global
821 change on Karst groundwater mineralization in the Jura mountains, *Sci.*
822 *Total Environ.* 541 (2016) 1208–1221.
- 823 [26] Y. Wang, A. Sergent, D. Saury, D. Lemonnier, P. Joubert, Numerical
824 study of an unsteady confined thermal plume under the influence of gas
825 radiation, *Int. J. Therm. Sci.* 156 (2020) 106474.
- 826 [27] M. Delort-Laval, L. Soucasse, P. Rivière, A. Soufiani, Rayleigh–Bénard
827 convection in a cubic cell under the effects of gas radiation up to $Ra=10^9$,
828 *Int. J. Heat Mass Transfer* 187 (2022) 122453.
- 829 [28] K. Lari, M. Baneshi, S. A. Gandjalikhan Nassab, A. Komiya,
830 S. Maruyama, Combined heat transfer of radiation and natural con-
831 vection in a square cavity containing participating gases, *Int. J. Heat*
832 *Mass Transfer* 54 (2011) 5087–5099.
- 833 [29] Y. Billaud, D. Saury, D. Lemonnier, Numerical investigation of coupled
834 natural convection and radiation in a differentially heated cubic cavity
835 filled with humid air. Effects of the cavity size., *Numer. Heat Transfer,*
836 *Part A* 72 (2017) 495–518.
- 837 [30] L. Soucasse, Ph. Rivière, A. Soufiani, S. Xin, P. Le Quéré, Transitional
838 regimes of natural convection in a differentially heated cavity under the
839 effects of wall and molecular gas radiation, *Physics of Fluids* 26 (2014)
840 024105.
- 841 [31] L. Soucasse, Ph. Rivière, A. Soufiani, Natural convection in a differen-
842 tially heated cubical cavity under the effects of wall and molecular gas
843 radiation at Rayleigh numbers up to 3×10^9 , *Int. J. Heat Fluid Flow*
844 61-B (2016) 510–530.
- 845 [32] T. Kogawa, J. Okajima, A. Sakurai, A. Komiya, S. Maruyama, Influence
846 of radiation effect on turbulent natural convection in cubic cavity at
847 normal temperature atmospheric gas, *Int. J. Heat Mass Transfer* 104
848 (2017) 456–466.
- 849 [33] T. Kogawa, L. Chen, J. Okajima, A. Sakurai, A. Komiya, S. Maruyama,
850 Effects of concentration of participating media on turbulent natural con-
851 vection in cubic cavity, *Appl. Therm. Eng.* 131 (2018) 141–149.

- 852 [34] N. Peyraube, R. Lastennet, A. Denis, P. Malaurent, N. Houillon, J.-D.
853 Villanueva, Determination and quantification of major climatic param-
854 eters influencing the CO₂ of Lascaux Cave, *Theor. Appl. Climatol.* 133
855 (2018) 1291–1301.
- 856 [35] G. Badino, Clouds in caves, *Speleogenesis and evolution of karst aquifer*
857 2 (2004) 1–8.
- 858 [36] J. Dredge, I. Fairchild, R. Harrison, A. Fernandez-Cortes, S. Sanchez-
859 Moral, V. Jurado, J. Gunn, A. Smith, C. Spötl, D. Matthey, P. Wynn,
860 N. Grassineau, Cave aerosols: distribution and contribution to
861 speleothem geochemistry, *Quat. Sci. Rev.* 63 (2013) 23–41.
- 862 [37] G. Barnes, The effect of monolayers on the evaporation of liquids, *Ad-
863 vances in colloid and interface science* 25 (1986) 89–202.
- 864 [38] I. Gordon, L. Rothman, C. Hill, R. Kochanov, Y. Tan, P. Bernath,
865 M. Birk, V. Boudon, A. Campargue, K. Chance, B. Drouin, J.-M.
866 Flaud, R. Gamache, J. Hodges, D. Jacquemart, V. Perevalov, A. Perrin,
867 K. Shine, M.-A. Smith, J. Tennyson, G. Toon, H. Tran, V. Tyuterev,
868 A. Barbe, A. Császár, V. Devi, T. Furtenbacher, J. Harrison, J.-M.
869 Hartmann, A. Jolly, T. Johnson, T. Karman, I. Kleiner, A. Kyuberis,
870 J. Loos, O. Lyulin, S. Massie, S. Mikhailenko, N. Moazzen-Ahmadi,
871 H. Müller, O. Naumenko, A. Nikitin, O. Polyansky, M. Rey, M. Rotger,
872 S. Sharpe, K. Sung, E. Starikova, S. Tashkun, J. V. Auwera, G. Wagner,
873 J. Wilzewski, P. Wcisło, S. Yu, E. Zak, The HITRAN2016 molecular
874 spectroscopic database, *Journal of Quantitative Spectroscopy and*
875 *Radiative Transfer* 203 (2017) 3–69, HITRAN2016 Special Issue.
876 doi:<https://doi.org/10.1016/j.jqsrt.2017.06.038>.
877 URL <https://www.sciencedirect.com/science/article/pii/S0022407317301073>
- 878 [39] W. Rohsenow, J. Hartnett, Y. Cho, *Handbook of heat transfer*, McGraw-
879 Hill (1998).
- 880 [40] S. Xin, P. Le Quéré, An extended Chebyshev pseudo-spectral benchmark
881 for the 8:1 differentially heated cavity, *Numerical Methods in Fluids* 40
882 (2002) 981–998.
- 883 [41] S. Xin, J. Chergui, P. Le Quéré, 3D spectral parallel multi-domain com-
884 puting for natural convection flows, in: Springer (Ed.), *Parallel Compu-*

- 885 tational Fluid Dynamics, Lecture Notes in Computational Science and
886 Engineering book series, Vol. 74, 2008, pp. 163–171.
- 887 [42] E. Tadmor, Convergence of spectral methods for nonlinear conservation
888 laws, *SIAM J. Numer. Anal.* 26 (1) (1989) 30–44.
- 889 [43] G. S. Karamanos, G. E. Karniadakis, A spectral vanishing viscosity
890 method for large-eddy simulations, *Journal of Computational Physics*
891 163 (2000) 22–50.
- 892 [44] R. Pasquetti, Spectral vanishing viscosity method for large-eddy sim-
893 ulation of turbulent flows, *Journal of Scientific Computing* 27 (2006)
894 365–375.
- 895 [45] L. Pierrot, P. Rivière, A. Soufiani, J. Taine, A fictitious-gas-based ab-
896 sorption distribution function global model for radiative transfer in hot
897 gases, *Journal of Quantitative Spectroscopy and Radiative Transfer* 62
898 (1999) 609–624.
- 899 [46] L. Soucasse, Ph. Rivière, S. Xin, P. Le Quéré, A. Soufiani, Numerical
900 study of coupled molecular gas radiation and natural convection in a
901 differentially heated cubical cavity, *Comput. Therm. Sci.* 4 (2012) 335–
902 350.
- 903 [47] L. Soucasse, Ph. Rivière, A. Soufiani, Subgrid-scale model for radia-
904 tive transfer in turbulent participating media, *Journal of Computational*
905 *Physics* 257, Part A (2014) 442–459.
- 906 [48] L. Soucasse, B. Podvin, Ph. Rivière, A. Soufiani, Low-order models for
907 predicting radiative transfer effects on Rayleigh-Bénard convection in a
908 cubic cell at different rayleigh numbers, *Journal of Fluid Mechanics* 917
909 (2021) A5.
- 910 [49] T. Kogawa, E. Shoji, J. Okajima, A. Komiya, S. Maruyama, Experimen-
911 tal evaluation of thermal radiation effects on natural convection with a
912 rayleigh number of $10^8 - 10^9$ by using an interferometer, *Int. J. Heat*
913 *Mass Transfer* 132 (2019) 1239–1249.
- 914 [50] W. White, Chemistry and karst, *Acta Carsologica* 440 (2015) 349–362.

- 915 [51] B. Lopez, Les processus de transfert d'eau et de dioxyde de carbone
916 dans l'épikarst, Ph.D. thesis, Université Bordeaux 1 (2009).
- 917 [52] C. R. de Freitas, A. Schmekal, Studies of condensation/evaporation pro-
918 cess in the Glowworm Cave, New Zealand, *Int. J. Speleol.* 35 (2006)
919 75–81.
- 920 [53] R. Buecher, Pre-development studies at Kartchner Caverns, in: *National*
921 *Cave Management Symposium Proceedings*, Bowling Green, Kentucky,
922 1991, pp. 144–163.
- 923 [54] V. N. Dublyansky, Y. V. Dublyansky, The problem of condensation in
924 karst studies, *J. Cave Karst Studies* 60 (1998) 3–17.
- 925 [55] D. Cailhol, P. Audra, C. Nehme, F. H. Nader, M. Garašić, V. Heresanu,
926 S. Gucel, I. Charalambidou, L. Satterfield, H. Cheng, R. L. Edwards,
927 The contribution of condensation–corrosion in the morphological evo-
928 lution of caves in semi-arid regions: preliminary investigations in the
929 Kyrenia Range, Cyprus, *Acta Carsologica* 48 (2019) 5–27.
- 930 [56] A. Belmonte, A. Tilgner, and A. Libchaber, Temperature and velocity
931 boundary layers in turbulent convection, *Phys. Rev. E*, 50 (1994) 269–
932 279.
- 933 [57] W.H. Leong, K.G.T. Hollands, and A.P. Brunger, Experimental Nusselt
934 numbers for a cubical-cavity benchmark problem in natural convection,
935 *Int. J. Heat Mass Transfer*, 42 (1999) 1979–1989.
- 936 [58] L. Soucasse, Effets des transferts radiatifs sur les écoulements de con-
937 vection naturelle dans une cavité différentiellement chauffée en régimes
938 transitionnel et faiblement turbulent, PhD thesis, École Centrale Paris,
939 France, 2013.